NASA/TM-2007-214627

Lunar Return Reentry Thermal Analysis of a Generic Crew Exploration Vehicle Wall Structures

William L. Ko, and Van T. Tran
NASA Dryden Flight Research Center
Edwards, California

Jeff Bowles
NASA Ames Research Center
Moffett Field, California

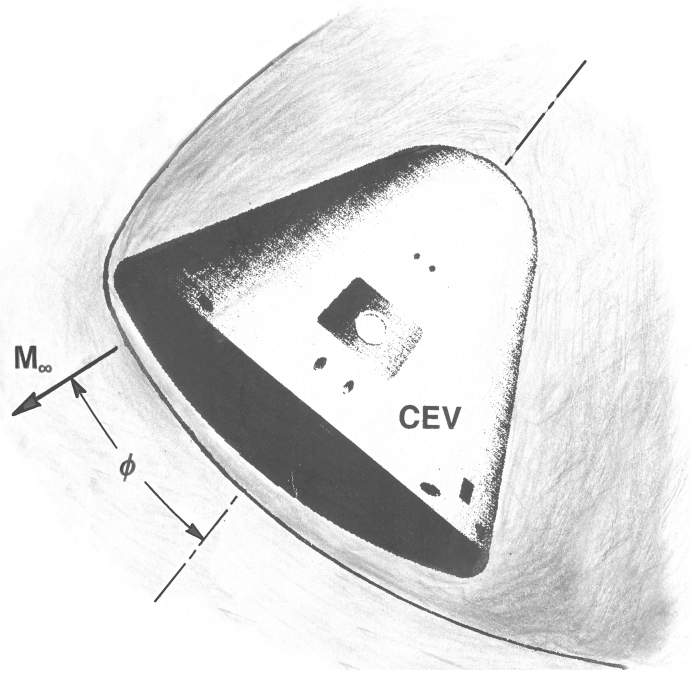

October 2007

NASA STI Program ... in Profile

Since its founding, NASA has been dedicated to the advancement of aeronautics and space science. The NASA scientific and technical information (STI) program plays a key part in helping NASA maintain this important role.

The NASA STI program is operated under the auspices of the Agency Chief Information Officer. It collects, organizes, provides for archiving, and disseminates NASA's STI. The NASA STI program provides access to the NASA Aeronautics and Space Database and its public interface, the NASA Technical Report Server, thus providing one of the largest collections of aeronautical and space science STI in the world. Results are published in both non-NASA channels and by NASA in the NASA STI Report Series, which includes the following report types:

- TECHNICAL PUBLICATION. Reports of completed research or a major significant phase of research that present the results of NASA programs and include extensive data or theoretical analysis. Includes compilations of significant scientific and technical data and information deemed to be of continuing reference value. NASA counterpart of peer-reviewed formal professional papers but has less stringent limitations on manuscript length and extent of graphic presentations.

- TECHNICAL MEMORANDUM. Scientific and technical findings that are preliminary or of specialized interest, e.g., quick release reports, working papers, and bibliographies that contain minimal annotation. Does not contain extensive analysis.

- CONTRACTOR REPORT. Scientific and technical findings by NASA-sponsored contractors and grantees.

- CONFERENCE PUBLICATION. Collected papers from scientific and technical conferences, symposia, seminars, or other meetings sponsored or cosponsored by NASA.

- SPECIAL PUBLICATION. Scientific, technical, or historical information from NASA programs, projects, and missions, often concerned with subjects having substantial public interest.

- TECHNICAL TRANSLATION. English-language translations of foreign scientific and technical material pertinent to NASA's mission.

Specialized services also include creating custom thesauri, building customized databases, and organizing and publishing research results.

For more information about the NASA STI program, see the following:

Access the NASA STI program home page at *http://www.sti.nasa.gov.*

- E-mail your question via the Internet to help@sti.nasa.gov.

- Fax your question to the NASA STI Help Desk at (301) 621-0134.

- Phone the NASA STI Help Desk at (301) 621-0390.

- Write to:
  NASA STI Help Desk
  NASA Center for AeroSpace Information
  7115 Standard Drive
  Hanover, MD 21076-1320

NASA/TM-2007-214627

Lunar Return Reentry Thermal Analysis of a Generic Crew Exploration Vehicle Wall Structures

William L. Ko, and Van T. Tran
NASA Dryden Flight Research Center
Edwards, California

Jeff Bowles
NASA Ames Research Center
Moffett Field, California

National Aeronautics and
Space Administration

Dryden Flight Research Center
Edwards, California 93523-0273

October 2007

Acknowledgment

The authors gratefully acknowledge the contributions of Mr. Joel Broome and Mr. Michael Tigges of the Flight Mechanics and Trajectory Design Branch, NASA Johnson Space Center, in generating different lunar and low Earth orbit reentry trajectories for reentry heating calculations.

Cover art: NASA Dryden Flight Research Center, art number 070263.

Available from:

NASA Center for AeroSpace Information
7115 Standard Drive
Hanover, MD 21076-1320
(301) 621-0390

CONTENTS

ABSTRACT

Thermostructural analysis was performed on generic crew exploration vehicle (GCEV) heat shielded wall structures subjected to reentry heating rates based on five potential lunar return reentry trajectories. The GCEV windward outer wall is fabricated with a graphite/epoxy composite honeycomb sandwich panel and the inner wall with an aluminum honeycomb sandwich panel. The outer wall is protected with an ablative Avcoat-5026-39H/CG thermal protection system (TPS). A "virtual ablation" method (a graphical approximation) developed earlier was further extended, and was used to estimate the ablation periods, ablation heat loads, and the TPS recession layer depths.

It was found that up to 83–95 percent of the total reentry heat load was dissipated in the TPS ablation process, leaving a small amount (3–15 percent) of the remaining total reentry heat load to heat the virgin TPS and maintain the TPS surface at the ablation temperature, 1,200ºF. The GCEV stagnation point TPS recession layer depths were estimated to be in the range of 0.280–0.910 in, and the allowable minimum stagnation point TPS thicknesses that could maintain the substructural composite sandwich wall at the limit temperature of 300°F were found to be in the range of 0.767–1.538 in.

Based on results from the present analyses, the lunar return abort ballistic reentry was found to be quite attractive because it required less TPS weight than the lunar return direct, the lunar return skipping, or the low Earth orbit guided reentry, and only 11.6 percent more TPS weight than the low Earth orbit ballistic reentry that will encounter a considerable weight penalty to obtain the Earth orbit. The analysis also showed that the TPS weight required for the lunar return skipping reentry was much more than the TPS weight necessary for any of the other reentry trajectories considered.

NOMENCLATURE

a	thermal absorptivity
CBAERO	Configuration Based Aerothermodynamics
CEV	crew exploration vehicle
CFD	computational fluid dynamics
C41	four nodes convection element
c	height of windward spherical wall, in
c_p	specific heat, Btu/lb-ºF
D	diameter, in
DPLR	data-parallel line relaxation
EI	entry interface
FRSI	Felt Reusable Surface Insulation
GCEV	generic crew exploration vehicle

h	TPS thickness, in
h_c	honeycomb core depth, in
$h_{\min}$	$= \delta_{\max} + h_V$, minimum TPS thickness required to keep substructure within design limit temperature of 300ºF, in
h_V	minimum virgin TPS thickness required to stay within design limit temperature, in
JLOC	joint location (node)
K41	four nodes conduction element
K81	eight nodes conduction element
k_1, k_2, k_3	thermal conductivities in 1,2,3 directions, Btu/in-sec-ºF
k_L	thermal conductivity in fiber direction, Btu/in-sec-ºF
k_T	thermal conductivity normal to fiber direction, Btu/in-sec-ºF
L/D	lift-to-drag ratio
LEO	low Earth orbit
LR	lunar return
Q	total reentry heat load, Btu/in^2
$\dot{q}$	heating rate, Btu/in^2-sec
q_A	ablation heat load, Btu/in^2
q_C	conduction heat load (the heating required to heat the virgin TPS and maintain the TPS surface at the ablation temperature T_A), Btu/in^2
q_T	$= q_C + q_A$, total heat load over each ablation period, Btu/in^2
$\dot{q}_C$	conduction heating rate, Btu/in^2-sec
q_V	heat of vaporization, Btu/in^3
R	radius, in
R41	four nodes radiation element
r_c	radius of GCEV windward spherical wall, in
r	diffuse component of the total reflectivity
STS	Space Transportation System
T	temperature, °F, or °R
T_A	ablation temperature, °F
T_{SW}	substructural sandwich wall temperature, °F
TPS	thermal protection system
t	time, sec
t_1	single-phase (or phase 1) ablation starting time, sec
t_2	single-phase (or phase 1) ablation ending time, sec
t_1'	phase 2 ablation starting time, sec
t_2'	phase 2 ablation ending time, sec

W	initial windward TPS weight, lb
ΔW	vaporized TPS weight at any time step t, lb
$(\Delta W)_{max}$	maximum value of ΔW at end of flight, lb
δ	TPS recession layer thickness at any time step during ablation, in
δ_{max}	maximum TPS recession depth at end of ablation, in
ε	thermal emissivity
ρ	density, lb/in^3
ϕ	angle of tilt (angle between CEV axis and flight path), deg

INTRODUCTION

The future crew exploration vehicle (CEV) is designed to carry a four-person crew for approximately 16 days during a lunar mission. At the end of the exploration mission, the CEV capsule will reenter the Earth's atmosphere and return to the Earth with a nominal landing on land as the baseline landing mode. The contingency plan will be a water landing, similar to earlier Apollo missions. The geometry of the proposed CEV reentry capsule could be very similar to the shape of the earlier Apollo capsule, or much larger. The CEV reentry capsule structures must be designed to survive hostile reentry aerodynamic heating and mitigate the baseline land landing impact by jettisoning the heat shield and deploying some type of shock absorbing system before landing.

Since the Apollo era, various new advanced materials have been developed, some are far more efficient (low density, lightweight, high strength, low heat conduction) than the structural shell materials used in the Apollo capsule. Before beginning the construction of the CEV capsule, comparative studies of heat transfer characteristics and mechanical performance of the advanced candidate materials must be performed to determine the best materials for the proposed CEV reentry capsule.

The heat-shielding characteristics of the honeycomb sandwich panels was extensively investigated by Ko (ref. 1). In recent heat-shielding studies of honeycomb sandwich panels fabricated with different materials, Ko, Gong, and Quinn (ref. 2) found that the graphite/epoxy composite sandwich construction could be a promising candidate structure for the CEV wall. In addition, they also performed reentry heat-transfer analyses of a generic CEV capsule windward wall structures using Apollo low Earth orbit reentry trajectories (ref. 3), and developed a "virtual ablation" method (graphical approximation) to study the recession behavior of the ablative thermal protection system (TPS).

For this report, lunar return reentry thermal analyses were performed on generic CEV capsule windward wall structures. The main purpose of these analyses is to study the effects of different lunar reentry trajectories on the substructural temperatures and to provide an estimate of the required TPS thicknesses and weights required to keep the substructures within design limits. This report presents the results from the thermal analysis for three lunar-return reentry trajectories and two low Earth orbit reentry trajectories.

THE CREW EXPLORATION VEHICLE

The geometry of the proposed CEV reentry capsule is shown in figure 1. The outer mold line shape of the capsule is essentially a modified and scaled up version of the earlier Apollo capsule shape. The forebody (windward) outer surface is a shallow spherical cap with a 196.85 in (5.00 m) diameter (compared to the 154.00 in diameter of the Apollo capsule) and a 246.00 in (6.25 m) radius of curvature (compared to the 184.80 in radius of curvature of the Apollo capsule). The aft-body is a circular cone with a 30.25 deg side wall angle (compared to the 33.00 deg side wall angle of the Apollo capsule) measured from the axis of symmetry. The apex of the aft-body cone is rounded. The outer surface of the CEV capsule is protected with a thermal protection system (TPS) to keep the CEV substructures from overheating.

The CEV capsule is to reenter the Earth atmosphere at an angle of tilt, ϕ, in order to achieve a hypersonic lift-to-drag ratio, L/D = 0.5 during reentry (compared to L/D = 0.3 for the Apollo capsule, ref. 3). As the reentry flight angle of tilt ϕ increases, the stagnation point will migrate upward, and the heating rate will gradually increase from the zero-tilt spherical stagnation heating rate. Based on Apollo data (ref. 3), the heating rate at the top toroidal shoulder could reach as high as (1.38, 1.44) times the zero-tilt spherical stagnation point heating rate respectively for the ϕ = (18, 20) deg angles of tilt. On the other hand, the bottom toroidal shoulder could only reach (60, 40) percent of the zero-tilt spherical stagnation point heating rate respectively for the ϕ = (18, 20) deg angles of tilt.

The optimum (or minimum) TPS thickness for the CEV windward wall must be determined based on the worst heating rate and flight angle of tilt ϕ among all possible reentry trajectories. The optimum TPS thickness is defined as the TPS thickness that will protect the substructures from overheating beyond the limit temperature (300°F for composites), and maintain the interior crew compartment wall at a comfortable temperature during the entire reentry flight.

Additionally, there exists a structural problem that must be considered in the CEV capsule design. At the time of land impact, the shallow spherical shell (if not properly reinforced from the interior), will be bent inwardly (fig. 2). This flattening bending will in turn bend the toroidal shoulder panel joining the spherical shell and the after-body conical shell, reducing the radius of curvature of the toroidal shell. It is well known that the bending of the curved sandwich shell in a direction to reduce the radius of curvature will induce depth-wise compression in the honeycomb core. If the depth-wise compression is too severe, honeycomb cell wall could buckle, resulting in the collapsing of the honeycomb core. These honeycomb cell wall buckling problems were extensively studied by Ko (ref. 1). Thus, the outer and the inner shell of the crew compartment must be properly connected to improve structural rigidity.

Before the structural design concept of the CEV is finalized, a generic CEV must be envisioned and used for thermal analysis to understand the thermostructural performance of the generic CEV subjected to the different candidate lunar return reentry heating rates.

THE GENERIC CREW EXPLORATION VEHICLE

Figure 2 shows the generic crew exploration vehicle (GCEV) during a hypothetical reentry flight at ϕ degree angle of tilt. The wall structural concepts of the GCEV are based on the structural concepts of both the Apollo capsule (fig. 3) (Appendix A) and the Space Shuttle Orbiter cargo bay doors (fig. 4) (Appendix A). The GCEV capsule is a double-walled sandwich construction. The GCEV windward spherical surface has 246.0 in radius of curvature and is protected with Avcoat-5026-39H/CG TPS (used for Apollo TPS) with an ablation temperature of approximately 1,200ºF (ref. 4). The outer wall (next to the TPS) is a composite honeycomb sandwich panel fabricated with graphite/epoxy composite face sheets and NOMEX honeycomb core (similar to the Space Shuttle Orbiter cargo bay door composite honeycomb construction). The inner (crew cabin) wall is a honeycomb sandwich panel fabricated with 2219-T8XX aluminum face sheets and honeycomb core (the same material used in the Space Shuttle Orbiter structures). The dimensions of the GCEV windward wall are indicated in the inset of figure 2. Both the outer and inner sandwich walls have the same core depth of 0.5 in, and the same face sheets thickness of 0.01 in. The two walls are separated by a 2 in gap of empty space (fig. 2 inset).

THE FUNCTION OF ABLATION

The function of ablative TPS is to dissipate a large portion of the heat load through decomposition, charring, and vaporization of the top layer of the TPS and, therefore, reduce the heat load entering the underlying virgin TPS and substructures. The Apollo capsule (ref. 3) used the ablative TPS material Avcoat-5026-39H/CG which has ablation temperature of approximately 1,200ºF (ref. 4). This implies that through ablation, the Apollo TPS surface temperature could never exceed 1,200ºF. If the ablation effect is ignored, Ko, Gong, and Quinn showed that the Apollo TPS surface temperature could exceed 3,000ºF under the Apollo low Earth orbit reentry heating (ref. 2). This shows how effective the ablation process is in lowering the TPS surface temperatures.

Figure 5 (ref. 5) shows the energy accommodations of the ablative TPS. Under extreme heat fluxes, the ablative TPS material can absorb large amounts of heat loads through phase change (charring) and shedding masses (ablation). The ablated TPS consists of a porous charred outer layer, pyrolysis sublayer (material decomposition by heat), and an inner virgin layer.

The total applied heat load during the ablation period may roughly be decomposed into two major components.

1. Conduction heat load (q_C): the heating required to heat the virgin TPS and maintain the TPS surface at the ablation temperature T_A. The conduction heat load includes the conduction heat loss, the heat losses through external and internal radiation, and heat loss through internal convection.
2. Ablation heat load $\left(q_A\right)$: for out-gassing, pyrolysis decomposition, and charring of the TPS.

The detailed discussions of the conduction and ablation heat loads (q_C, q_A), and the method of determining the values of (q_C, q_A) are presented respectively in the VIRTUAL ABLATION ANALYSIS section and the REENTRY HEATING section.

REENTRY HEATING

Five typical candidate lunar return (LR) and low Earth orbit (LEO) entry trajectories (velocities, altitudes, angles of tilt) were considered for the GCEV reentry thermostructural analysis. The lunar return reentry trajectory set consisted of two nominal entry trajectories (lunar-guided direct and lunar-guided skipping return) and an abort ballistic return. For the low Earth orbit return, the trajectory set consisted of a nominal guided entry and an abort ballistic entry. For both abort entries, the capsule has a high rate of bank angle, resulting in essentially a zero-lift entry.

Reentry Trajectories

The basic techniques to return a vehicle like the CEV from the moon to Earth could be direct entry, skipping entry, aerocapture followed by direct entry after one orbit, or aerocapture followed by direct entry after several orbits. Williams, et al (ref. 6) discusses those lunar return reentry trajectories and the associated reentry heating rates in great detail. Current plans for CEV entry call for a skipping trajectory for nominal lunar return. The skip trajectory being planned assumes an initial entry, followed by a short exo-atmospheric phase, then a second (direct) entry. The current CEV trajectory set may have different entry interface (EI) flight conditions compared to those presented in reference 6 (The EI for the Space Shuttle Orbiter is 400,000 ft altitude, ref. 7).

Figures 7–11 respectively show five cases of candidate lunar return and low Earth orbit reentry trajectories for the CEV generated by Mr. Joel Broome and Mr. Michael Tigges of the Flight Mechanics and Trajectory Design Branch at the NASA Johnson Space Center (Houston, Texas). The five cases of lunar return and low Earth orbit reentry trajectories for the calculations of the reentry heating rates for the CEV are listed below.

1. LR abort ballistic reentry trajectory (fig.7)
2. LR guided direct reentry trajectory (fig. 8)
3. LR guided skipping reentry trajectory (fig. 9)
4. LEO abort ballistic reentry trajectory (fig. 10)
5. LEO guided reentry trajectory (fig. 11)

For all of the candidate reentry cases, the CEV reentry angles of tilt, ϕ, stay at approximately ϕ = 27 deg during most part of the reentry flight and then increase slightly toward the end of flight. The lunar return ballistic reentry case (fig. 7) has monotonically decreasing velocity and altitude curves and has the shortest flight duration among the five reentry cases. The lunar return

direct reentry case (fig. 8), exhibits a modest skip in altitude after the initial entry phase. For the lunar return skipping reentry case (fig. 9), the vehicle skips back to approximately the initial entry altitude, with a decrease in velocity to less than the orbital speed. During the skipping phase, the velocity is roughly constant (conservation of total mechanical energy during low freestream dynamic pressure flight). For the low Earth orbit ballistic reentry case (fig. 10), altitude curve decreases monotonically, and the reentry velocity is almost constant during the high altitude/low dynamic pressure portion of the flight. Notice that the velocity and altitude curves of the low Earth orbit guided reentry case (fig. 11) are very similar to those of the Space Shuttle Orbiter reentry case (ref. 7).

To assess the total heat soak to the TPS and underlying support structure, the total flight time must be known. Only the lunar return skipping entry trajectory included the parachute deployment phase of the flight. The total flight times to touchdown were estimated for the remaining trajectories by adding the incremental time determined from the complete skipping entry profile. The touchdown times for the five reentry trajectories are listed in table 1. The actual touchdown times will depend upon the parachute deployment schedule for each flight.

Table 1. Estimated touchdown times for different flight trajectories.

	Touchdown time, sec
LR abort ballistic reentry	540 (shortest flight time)
LR guided direct reentry	936
LR guided skipping reentry	2,052* (longest flight time)
LEO abort ballistic reentry	760
LEO nominal guided reentry	1,090

* Actual time from trajectory print out.

Heating Rates Calculations

Based on the five cases of reentry trajectories shown in figures 7–11, the reentry heating rates for the CEV stagnation point were computed by interpolating the aerothermal database generated by CBAERO (Configuration Based Aerothermodynamics, refs. 8, 9) as a function of Mach number, freestream dynamic pressure and angle of tilt every one second along the flight path. The CBAERO code is an engineering-based computational code for predicting aerodynamics and aerothermodynamics of hypersonic vehicles (ref. 8, 9). Convective stagnation region heating is based on a Fay-Riddell type model with a modified Lee's distribution (ref. 10). Acreage heating is computed using a shock-expansion method to a local surface pressure determined using independent panel methods (tangent cone/wedge, Newtonian), coupled with a Reference-Enthalpy model (ref. 10). Running lengths are computed from the stagnation point and attachment line using the Newtonian surface streamlines. The shock layer radiation heating is computed using the engineering methods presented in reference 11. The engineering-based heating rates are anchored at selected flight conditions to high-fidelity CFD (computational fluid dynamics) computed solutions using the NASA Ames DPLR (data-parallel line relaxation) code (ref. 12). The total heating

environment consisted of both the convective heating and the shock layer radiation heating as a function of time and location on the vehicle surface. The heating rates were computed assuming the surface temperature was at the radiation equilibrium temperature. If required, the radiation equilibrium wall temperature could be computed with calculations of the energy balance at the surface using the film coefficient (blowing effects included) and the recovery enthalpy. No margins were applied to the aerothermal heating environments.

The calculated reentry stagnation point heating curves for the five cases of reentry trajectories presented are shown respectively in figures 12–16. The five reentry heating rates were then input to the thermal model for structural temperature calculations and virtual ablation analysis.

As expected, the heating curve for both the lunar return ballistic reentry heating case (fig. 12) and the low Earth orbit ballistic reentry heating case (fig. 15), has only one peak. The guided reentry heating cases (figs. 13, 14, 16) however, have one primary and one secondary peak heating rate. The peak heating rates, peak heating times, heating durations, and total heat loads of the five reentry heating cases are listed in table 2.

Table 2. Peak heating rates, peak heating time steps, heating durations, and total heat loads.

	Peak heating rate, Btu/in^2-sec	Peak heating time from reentry, sec	Heating duration, sec	Total heat load, Btu/in^2
LR abort ballistic reentry	2.5556 (highest)	74	200 (shortest)	129.91
LR guided direct reentry	2.2937	77	600	223.63
LR guided skipping reentry	2.1679	76	1800 (longest)	214.91
LEO abort ballistic reentry	0.4719	331	450	74.79
LEO nominal guided reentry	0.3097	270	800	102.08

The data in table 2 shows that the lunar return abort ballistic reentry has the highest heating rate and shortest heating duration. The results presented in table 2 also show that this lunar return trajectory has a total heating load much less than the two other lunar return trajectories, with the lunar return direct reentry having a slightly higher total heat load than the lunar return skipping reentry. The two low Earth orbit reentries had peak heating rates and total heat loads that were less than the lunar return reentries. It is quite interesting however, that the total heat loads for the low Earth orbit ballistic and low Earth orbit guided reentries are only 42.4 percent and 21.4 percent lower than the lunar return abort ballistic reentry.

THERMAL MODELING

For the heat transfer analysis, the structural performance and resizing (SPAR) finite element computer program (ref. 13) was used. For this purpose, a simple plug finite-element thermal model (fig. 6) was generated to model the GCEV stagnation point wall structures. This thermal model was used to study the heat-shielding performance of the TPS (i.e., the effect of TPS thickness on the substructural composite wall temperatures) and the virtual ablation thermal analysis.

In the simple plug thermal model, the TPS was modeled with 12 layers of eight nodes brick elements (K81 elements). Each of the face sheets and honeycomb core of the outer composite sandwich wall and inner aluminum sandwich wall were modeled with one layer of K81 element. The internal and external radiation exchanges are modeled with four nodes radiation elements (R41 elements). The inner aluminum sandwich wall was kept at 70°F to serve as a heat sink. The convection in the empty space was modeled with four nodes convection elements (C41 elements) connecting the outer and inner sandwich walls. All the input thermal properties of the materials used in the thermal model for the GCEV wall structures are listed in Appendix B. The TPS thickness, h, was varied in the range of $0.6 \le h \le 2.8$ in (maximum thickness of the Apollo TPS) to study the TPS heat-shielding performance. The size of the simple plug thermal model is listed in table 3.

Table 3. Size of simple plug thermal model.

	JLOC	K41	K81	R41	C41
Count	84	1	18	4	6

The heat inputs used in the thermal model (fig. 6) were the five candidate lunar return reentry heating rates described earlier (figs. 12–16).

HEAT TRANSFER ANALYSIS

The heat transfer analysis was carried out simultaneously with the virtual ablation analysis. It consists of the following major stages.

Pre-ablation Stage

The purpose of the pre-ablation heat transfer analysis is to determine the ablation starting time step. The pre-ablation thermal analysis was carried out only up to a certain time step. Then, the output TPS surface temperature was plotted as a function of time. When the TPS surface temperature curve intersects the horizontal ablation temperature (1,200ºF) line, the intersection time step was considered as the ablation starting time step. This is graphically illustrated in the VIRTUAL ABLATION ANALYSIS section.

Ablation Stage

The ablation stage of heat transfer analysis simultaneously determines the conduction heating rate for heating, maintains the TPS surface at a 1,200ºF ablation temperature over the ablation period, and determines the ablation ending time. The details of the graphical ablation analysis are presented in the VIRTUAL ABLATION ANALYSIS section.

Structural Temperature Calculations

After the conduction heating curve was established for the ablation period of each heating case, the revised heating curve (formed by replacing the ablation region of the original reentry heating curve with the conduction curve) was used to calculate the structural temperatures. See detailed discussions in the STRUCTURAL TEMPERATURES section.

VIRTUAL ABLATION ANALYSIS

The virtual ablation analysis is a graphical approximation method (aided by SPAR thermal analysis) developed for TPS ablation analysis. The virtual ablation method was developed earlier (ref. 2), and was further extended for longer reentry durations as described in the following sections.

Types of Heat Loads

During initial pre-ablation heating cycle, the total heat load is used to heat the virgin TPS surface to the ablation temperature, 1,200ºF. Once the TPS surface temperature has reached 1,200ºF, part of the reentry heat load is required to maintain this temperature during the ablation period. This portion of the heat load consist of the heat conducted into the TPS and substructure, the heat capacity of the TPS and substructures, the heat radiated away from the surface of the TPS, and the heat loss to the interior heat sink (crew cabin) by internal radiation and convection. In the present analysis, this portion of the heat load is called the conduction heat load, q_C (Btu/in^2). The remaining heat load during the time the surface temperature is above 1,200°F can be used in the ablation of the TPS and is called the ablation heat load, q_A (Btu/in^2). The total heat load, q_T (Btu/in^2) during the ablation period then consists of the conduction heat load, q_C, plus the ablation heat load, q_A, and described by equation (1).

$$q_T = q_C + q_A \tag{1}$$

To determine the ablation period heat loads, $\{q_T, q_C, q_A\}$, one must first know the ablation starting and ending times, and the associated conduction heating rate, $\dot{q}_C$, for each ablation period. With those values determined, the area under each heating curve (figs. 12–16) and area under each conduction heating curve bounded by the ablation starting and ending times will give the total and conduction heat loads $\{q_T, q_C\}$. The ablation heat load, q_A, may then be calculated from equation (1). The calculations of the heat loads $\{q_T, q_C, q_A\}$ are presented in the sections called CALCULATIONS OF HEAT LOADS.

Thermal Protection System Surface Temperature Curves

Figures 17–21 respectively show the TPS surface temperature time histories based on the outputs of the SPAR thermal analysis. To conduct the virtual ablation analysis, the reentry heating curves (figs. 12–16) were also plotted respectively in figures 17–21. Each set of heating and temperature curves (figs. 17–21) was then used to graphically determine the ablation starting time, ablation ending times, and the conduction heating rate for heating and maintaining the virgin TPS surface at the ablation temperature, 1,200ºF over each ablation period.

Ablation Starting Times

In each of figures 17–21, the initial heat load (area under the heating curve portion 0A was used to heat the TPS surface up to 1,200ºF at $t = t_1$. After $t = t_1$ the TPS surface temperature will continue to rise and exceed 1,200°F if the TPS is assumed to be non-ablative. Therefore, the time step $t = t_1$ could be considered as the ablation starting time. The ablation ending time, t_2, is not yet known. As shown in the subsequent sections, t_2 could be determined once the correct conduction-heating curve from point B to point C, (figs. 17–21) is established.

For the reheating phase of skipping reentry case (phase 2 ablation period, fig. 19), the heat load (area under the heating curve portion rising from zero-heating point up to point B') will reheat the TPS surface up to 1,200°F again at $t = t_1'$ (point B'). The time step $t = t_1'$ is then considered as the phase 2 ablation starting time. Similar to phase 1 ablation, the phase 2 ablation ending time t_2' can be determined only after the correct conduction-heating curve $B'C'$ (fig. 19) is established.

Conduction Heating Rates

After $t = t_1$, one must first determine the portion of the heat load (for example, the conduction heat load) not directed towards the ablation process. This conduction heat load, q_C (Btu/in^2), will be used to continue to heat the TPS and maintain the TPS surface temperature at 1,200ºF over the ablation period. The rest of the heat load, q_A (Btu/in^2), is then used to ablate the TPS.

To find the correct conduction heating rate to heat and maintain the TPS surface temperature at 1,200ºF for each ablation period, repeated finite-element heat transfer analyses had to be carried out using different trial conductive heating rates until the output TPS surface temperatures converged to 1,200ºF over each ablation period. The TPS surface temperatures calculated using the revised heating curve are plotted in figures 17–21 with solid circular symbols. Note that the correct conduction heating rate caused the data point to fall practically on the 1,200ºF temperature line over each ablation period.

As shown in figures 17–21 the correct conduction heating curve for each ablation period was found to be a slightly tilted straight line depicted by the BC line for the single-phase ablation (or for phase 1 ablation of the skipping reentry case, fig. 19), starting with heating rate, $\dot{q}_C(t_1)$, at point B ($t = t_1$) decreases slightly to $\dot{q}_C(t_2)$ at point C ($t = t_2$) lying on the reentry heating curve. Because the interior of the intact TPS is gradually heated with time, less and less conduction

heating rate is required to maintain the TPS surface temperature at 1,200°F and, therefore, the BC line slightly tapers down toward point C. Beyond point C, ablation process should end because the reentry heating rate is now less than the conduction heating rate, $\dot{q}_C$ (there is no more excess heat energy for ablation).

Likewise, the correct conduction heating line $\mathrm{B'C'}$ for phase 2 ablation of the skipping reentry case (fig. 19) starts with heating rate, $\dot{q}_C(t_1')$, at point $\mathrm{B'}$ ($t = t_1'$) and decreases slightly to $\dot{q}_C(t_2')$ at point $\mathrm{C'}$ ($t = t_2'$) lying on the reentry heating curve. The conduction heating rates $\{\dot{q}_C(t_1'),\ \dot{q}_C(t_2')\}$ at points $\{\mathrm{B'C'}\}$ for phase 2 ablation in figure 19 were found to be slightly less than $\{\dot{q}_C(t_1),\ \dot{q}_C(t_2)\}$ at points $\{\mathrm{B'C'}\}$ of phase 1 ablation.

The conduction heating rate, $\dot{q}_C(t)$ at any time, t, along line BC of single-phase or phase 1 ablation (figs. 17–21) may be expressed as the linearly decreasing function of time in terms of the known $\{\dot{q}_C(t_1),\ \dot{q}_C(t_2)\}$ respectively at points {B, C} as shown in equation (2).

Conduction heating rate for single-phase (or phase 1) ablation:

$$\dot{q}_C(t) = \dot{q}_C(t_1) - [\dot{q}_C(t_1) - \dot{q}_C(t_2)]\frac{t - t_1}{t_2 - t_1} \tag{2}$$

Similarly, the conduction heating rate $\dot{q}_C(t)$ along line $\mathrm{B'C'}$ of phase 2 ablation (fig. 19) may be expressed in terms of the known conduction heating rates $\{\dot{q}_C(t_1'),\ \dot{q}_C(t_2')\}$ respectively at points $\{\mathrm{B'C'}\}$ as shown in equation (3).

Conduction heating rate for phase 2 ablation:

$$\dot{q}_C(t) = \dot{q}_C(t_1') - [\dot{q}_C(t_1') - \dot{q}_C(t_2')]\frac{t - t_1'}{t_2' - t_1'} \tag{3}$$

Through repeated finite-element thermal analysis, the correct value of $\dot{q}_C(t_1)$ at point B (phase 1 ablations) for all the five heating cases (figs. 17–21) was found to be $\dot{q}_C(t_1) = 0.032$ Btu/in^2-sec for Avcoat-5026-39H/CG (the Apollo TPS material). The conduction heating rate $\dot{q}_C(t_2)$ at point C is slightly less than 0.032 Btu/in^2-sec and varied with the reentry heating case.

Ablation Ending Times

As shown in figures 17–21, the time step $t = t_2$ at point C may be considered the ablation ending time, t_2, for single-phase ablation (or phase 1 ablation of the skipping reentry case, fig. 19). Likewise, the times $t = t_2'$ at point $\mathrm{C'}$ (fig. 19) may be considered as the phase 2 ablation ending time of the skipping reentry case (fig. 19).

Once the correct value of the conduction heating rates $\dot{q}_C(t_2)$ at point C [or $\dot{q}_C(t_2')$ at point $\mathrm{C'}$ (fig. 19)] is determined (figs. 17–21), the time step at point C (or $\mathrm{C'}$) will be considered as the

ablation ending time, t_2 (or t_2'). The time duration $t_1 - t_2$ (or $t_1' - t_2'$) may then be defined as the virtual ablation period.

Virtual Ablation Data Summary

The virtual ablation period data obtained from the SPAR thermal analysis and the graphical virtual ablation analysis for the five reentry heating cases are summarized in table 4.

Table 4. Data for the virtual ablation periods for different reentry heating cases.

Heating	Phase 1 ablation					Phase 2 ablation				
	t_1, sec	t_2, sec	$(t_2 - t_1)$, sec	$\dot{q}_C(t_1)$, Btu/in^2-sec	$\dot{q}_C(t_2)$, Btu/in^2-sec	t_1', sec	t_2', sec	$(t_1' - t_2')$, sec	$\dot{q}_C(t_1')$, Btu/in^2-sec	$\dot{q}_C(t_2')$, Btu/in^2-sec
LR abort ballistic reentry	28	166	**138***	0.032	0.03079					
LR guided direct reentry	27	503	476	0.032	0.02660					
LR guided skipping reentry										
(phase 1 ablation)	30	320	290	0.032	0.02587					
(phase 2 ablation)						1,285	1,649	364	0.029	0.02384
LEO abort ballistic reentry	118	394	276	0.032	0.02708					
LEO nominal guided reentry	121	652	**531**†	0.032	0.02440					

* Shortest ablation period

† Longest ablation period

Table 4 shows that the lunar return ballistic reentry case has the shortest ablation period of 138 seconds, and the low Earth orbit guided reentry case has the longest ablation period of 531 seconds.

CALCULATIONS OF HEAT LOADS

Once the ablation starting and ending times, $\{t_1, t_2\}$, and the correct conduction heating rate, $\dot{q}_C(t)$, over each ablation period are determined, the three heat loads, $\{q_T, q_C, q_A\}$, during the ablation period may be obtained by integrating the proper heating rate over the ablation period $t_1 \le t \le t_2$ (or $t_1' \le t \le t_2'$). The total heating load, q_T, for different ablation phases is to be calculated from equations (4) and (5).

For single-phase (or phase 1) ablation:

$$\begin{aligned} q_T &= \int_{t_1}^{t_2} \dot{q}(t)dt \\ &= \text{ area under the reentry heating curve bounded by } t_1 \text{ and } t_2 \end{aligned} \tag{4}$$

For phase 2 ablation:

$$\begin{aligned} q_T &= \int_{t_1}^{t_2} \dot{q}(t)dt + \int_{t_1'}^{t_2'} \dot{q}(t)dt \\ &= \text{ area under the reentry heating curve bounded by } t_1 \text{ and } t_2 \\ &\quad + \text{area under the reentry heating curve bounded by } t_1 \text{ and } t_2 \end{aligned} \tag{5}$$

The conduction heat load, q_C, for different ablation phases is to be calculated from equations (6) and (7).

For single-phase (or phase 1) ablation:

$$\begin{aligned} q_C &= \int_{t_1}^{t_2} \dot{q}_C(t)dt = \frac{1}{2}[\dot{q}_C(t_1) + \dot{q}_C(t_2)](t_2 - t_1) \\ &= \text{ area under the conduction heating curve BC bounded by } t_1 \text{ and } t_2 \end{aligned} \tag{6}$$

where equation (2) was used in carrying out the integration of $\dot{q}_C(t)$ over the phase 1 ablation period.

For phase 2 ablation:

$$\begin{aligned} q_C &= \int_{t_1}^{t_2} \dot{q}_C(t)dt + \int_{t_1'}^{t_2'} \dot{q}_C(t)di \\ &= \frac{1}{2}[\dot{q}_C(t_1) + \dot{q}_C(t_2)](t_2 - t_1) + \frac{1}{2}[\dot{q}_C(t_1') + \dot{q}_C(t_2')](t_2' - t_1') \\ &= \text{ area under the conduction heating curve BC bounded by } t_1 \text{ and } t_2 \\ &\quad + \text{area under the conduction heating curve B}'\text{C}' \text{ bounded by } t_1' \text{ and } t_2'.. \end{aligned} \tag{7}$$

where equations (2) and (3) were used for $\dot{q}_C(t)$ in carrying out the integrations over the phase 1 and phase 2 ablation periods respectively.

Ablation Heat Load

Once the total and conduction heat loads $\{q_T, q_C\}$ are determined, the ablation heat load q_A may then be easily obtained from equation (8).

$$q_A = q_T - q_C$$
$$= \text{area between the reentry heating curve and the conduction heating curves within the ablation periods} \quad (8)$$

Heat Loads Data Summary

The total reentry heat loads, Q (Btu/in^2) (from reentry to touchdown), and the three ablation period heat loads, $\{q_T, q_C, q_A\}$ (Btu/in^2), calculated from equations (4)–(8) for the five cases of reentry heating rates are listed in table 5.

Table 5. Heat loads for different reentry heating rates.

Trajectory	Q, Btu/in^2		q_T, Btu/in^2	q_C, Btu/in^2	q_A, Btu/in^2
LR abort ballistic reentry	129.91 (100%)		128.40 (98.84%)	4.35 (3.35%)	124.05 (95.49%)
LR guided direct reentry	223.63 (100%)		221.76 (99.16%)	14.04 (6.28%)	207.72 (92.88%)
LR guided skipping reentry					
(phase 1 ablation)	-----		147.00	8.39	138.61
(phase 2 ablation)	-----	+)	59.29	9.62	49.67
Total	214.91 (100%)		206.29 (95.99%)	18.01 (8.38%)	188.28 (87.61%)
LEO abort ballistic reentry	74.79 (100%)		72.36 (96.75%)	8.15 (10.90%)	64.21 (85.85%)
LEO nominal guided reentry	102.08 (100%)		99.22 (97.20%)	14.97 (14.67%)	84.25 (82.53%)

Note from table 5 that during the TPS ablation period, very small portions (3.35–14.67 percent) of the total reentry heat loads, Q, could penetrate into the intact TPS for conductive heating. Major portions (82.53–95.49 percent) of Q were removed through out-gassing of the ablation process. This is truly the beauty of the high performance heat-shielding characteristics of the ablative TPS material.

THERMAL PROTECTION SYSTEM RECESSION ANALYSIS

Once the ablation heat loads are determined, the TPS recession layer depths and the corresponding weight may be calculated. The following five sections show the TPS recession analysis.

Thermal Protection System Recession Layer Depths

Let q_V be the heat of vaporization (including charring) of the ablative TPS material, and t_1 be the ablation starting time, then the transient TPS recession layer thickness, $\delta(t)$, at any time, *t*, during the ablation period may be calculated from the partial ablation heat load, $\int_{t_1}^{t}[\dot{q}(t)-\dot{q}_C(t)]dt$ (Btu/in^2) divided by the heat of vaporization, q_V (Btu/in^3), for the single-phase (or phase 1) ablation. The transient TPS recession layer thickness, $\delta(t)$, is then calculated from equation (9).

For single-phase (or phase 1) ablation:

$$\begin{aligned}\delta(t) &= \frac{1}{q_V}\int_{t_1}^{t}[\dot{q}(t)-\dot{q}_C(t)]dt \\ &= \frac{1}{q_V}\left[\int_{t_1}^{t}\dot{q}(t)dt-\frac{1}{2}[\dot{q}_C(t_1)+\dot{q}_C(t)](t-t_1)\right] \qquad ; \quad t_1 \le t \le t_2 \end{aligned} \tag{9}$$

where equation (2) was used in carrying out the integration of $\dot{q}_C(t)$ up to time *t* ($t_1 \le t \le t_2$) within the single-phase ablation period.

During the phase 2 ablation, the cumulated partial ablation heat load takes on the form $\int_{t_1}^{t_2}[\dot{q}(t)-\dot{q}_C(t)]dt+\int_{t_1'}^{t}[\dot{q}(t)-\dot{q}_C(t)]dt$, and the cumulated TPS recession layer thickness, $\delta(t)$ is to be calculated from equation (10).

For phase 2 ablation:

$$\begin{aligned}\delta(t) &= \frac{1}{q_V}\left[\int_{t_1}^{t_2}[\dot{q}(t)-\dot{q}_C(t)]dt+\int_{t_1'}^{t}[\dot{q}(t)-\dot{q}_C(t)]dt\right] \\ &= \frac{1}{q_V}\left[\int_{t_1}^{t_2}\dot{q}(t)dt-\frac{1}{2}[\dot{q}_C(t_1)+\dot{q}_C(t_2)](t_2-t_1)\right] \qquad ; \quad t_1 \le t \le t_2 \\ &\quad +\frac{1}{q_V}\left[\int_{t_1'}^{t}\dot{q}(t)dt-\frac{1}{2}[\dot{q}_C(t_1')+\dot{q}_C(t)](t-t_1')\right]\end{aligned} \tag{10}$$

where equation (2) was used for $\dot{q}_C(t)$ in carrying out the integration over the phase 1 ablation period ($t_1 \le t \le t_2$), and equation (3) was used for $\dot{q}_C(t)$ in carrying out the integration up to time, *t*, within the phase 2 ablation period ($t_1' \le t \le t_2'$).

At the end of ablation ($t = t_2$ for single-phase ablation, or $t = t_2'$ for dual-phase ablation), the TPS recession layer thickness, $\delta(t)$, reaches a maximum $\delta(t_2) = \delta_{\max}$ (or $\delta(t_2') = \delta_{\max}$), which can be calculated from equation (9) or (10) by carrying out the integration up to the end of ablation $t = t_2$ (or $t = t_2'$). Alternatively, one can simply divide the ablation heat load, q_A, given in table 5 by the heat of vaporization, q_V, of the ablative TPS material as shown in equations (11) and (12).

For single-phase ablation:

$$\delta_{\max} = \delta(t_2) = \frac{q_{\mathrm{A}}(\text{phase 1})}{q_V} \tag{11}$$

For dual-phase ablation:

$$\delta_{\max} = \delta(t_2') = \frac{1}{q_V}\left[q_{\mathrm{A}}(\text{phase 1}) + q_{\mathrm{A}}(\text{phase 2})\right] \tag{12}$$

Thermal Protection System Recession Growth Curves

From table A1 of Appendix A, the heat of vaporization, q_V (including heat of decomposition), is given as q_V = 11,900 Btu/lb. Using the virgin density, $\rho = 1.9097 \times 10^{-2}\ \mathrm{lb/in^3}$ of the Avcoat-5026-39H/CG TPS material, the [Btu/lb] unit of q_V may be converted into [Btu/in^3] as $q_V = 11{,}900 \times 1.9097 \times 10^{-2} = 227.25\ \mathrm{lb/in^3}$.

Using the input value of $q_V = 227.25\ \mathrm{lb/in^3}$, the TPS recession layer thicknesses, $\delta(t)$, were calculated from equations (9) and (10) up to various time steps to generate the data set for plotting TPS recession growth curves. Figures 22–26 show $\delta(t)$ plotted as functions of time, *t*, for the five heating cases. For the lunar return ballistic reentry (fig. 22) and direct reentry (fig. 23), the TPS recession curves are somewhat S-shaped. The TPS recession rate increased rapidly during early stage of reentry and then the rate of increase slowed down and gradually reached the maximum values near touchdown. For the lunar return skipping reentry (fig. 24), each TPS recession growth curve has S-shapes similar to the previous two cases (figs. 22, 23). The phase 1 TPS recession rate is much higher than that of phase 2. There is a plateau (no ablation region) between the two phases of TPS recession growth curves.

For the low Earth orbit reentry cases (figs. 25, 26), the TPS recession growth curves are almost linear (especially fig. 25) except during the initial and final stages of reentry.

Thermal Protection System Recession Layer Weights

Let ρ be the density of the TPS material, r_c be the radius of the GCEV windward spherical wall, *c* be the height of the windward spherical wall, and *h* be the TPS thickness (assumed constant over the spherical wall). Then the weight *W* of the GCEV windward TPS may be calculated from equation (13).

$$W = \rho h(2\pi r_c c) \tag{13}$$

Using the following numerical input values for the present GCEV,

$\rho = 1.9097 \times 10^{-2}$ lb/in^3 (Apollo TPS material)

r_c = 246 in (approximately 6.25 m)

c = 21 in

equation (13) becomes equation (14).

$$W = 619.87h \quad \text{(lb)} \tag{14}$$

The weight $\Delta W(t)$ of the vaporized TPS layer at any time step t may then be calculated from equation (15).

$$\Delta W(t) = 619.87\delta(t) \quad \text{(lb)} \tag{15}$$

Thermal Protection System Recession Data Summary

Table 6 lists the maximum values of TPS recession layer thicknesses, δ_{max}, calculated from equations (11) or (12), and the associated maximum vaporized TPS weights, $(\Delta W)_{max}$, calculated from equation (15) using $\delta(t) = \delta_{max}$ as input. The values of total reentry heat loads, Q, and the ablation heat loads, q_A, are also listed for reference.

Table 6. Maximum TPS recession layer thicknesses, δ_{max}, and the maximum vaporized TPS weights, $(\Delta W)_{max}$.

Trajectory	Q, Btu/in^2	q_A, Btu/in^2	δ_{max}, in	$(\Delta W)_{max}$, lb
LR abort ballistic reentry	129.91	124.05	0.55	341.00
LR guided direct reentry	223.63*	207.72	0.91	564.20
LR guided skipping reentry	214.91	188.28	0.83	514.60
LEO abort ballistic reentry	74.79†	64.21	0.28	173.50
LEO nominal guided reentry	102.08	84.25	0.37	229.49

* Highest heat load

† Lowest heat load

Note from table 6 that by ablating only a thin surface layer of TPS, most of the reentry heat load could be expended, causing only a small amount of remaining heat load to penetrate into the intact TPS for conductive heating. Surely, the ablation process is an efficient way to remove a

major portion of the reentry heat load.

Thermal Protection System Recession Formulae

Figure 27 shows the maximum TPS recession layer thickness, δ_{max}, plotted as a function of the ablation heat load q_A. For this plot, the TPS recession thickness curve is a straight line passing through the origin, and is described by equation (16).

$$\delta_{max} = 0.0044 q_A \quad \text{(in)} \tag{16}$$

Figure 28 shows δ_{max} plotted as a function of the total reentry heat load, Q. For this plot, the data points do not form a perfect straight line, however, the data points do fall quite close to the straight line which can be described by equation (17).

$$\delta_{max} = 0.0040 Q \quad \text{(in)} \tag{17}$$

Equation (17) may be used to estimate the preflight TPS recession layer thickness for any reentry heating load, Q, without the need to perform virtual ablation analysis.

STRUCTURAL TEMPERATURES

As discussed, during the virtual ablation period, most of the heat load was consumed in ablating the TPS surface layer, leaving a small amount of the remaining heat load (area under curve BC in figs. 17, 18, 20, and 21 for a single-phase ablation case or areas under curves BC and B′C′ for the dual-phase ablation case, fig. 19) to heat and maintain the TPS surface temperature at 1,200°F over each ablation period. Therefore, in the calculations of the structural temperatures, the heat input was not based on the actual reentry-heating curve, but based on the conduction heating curve 0ABCD (figs. 17, 18, 20, 21) for a single-phase ablation case, or curve 0ABCB′C′D (fig. 19) for the dual-ablation case.

Structural Temperature Profiles

Figures 29–30 show the temperature distributions across the GCEV stagnation point wall at different time steps for the five reentry heating cases. In the temperature calculations, the TPS thickness of $h = 2.8$ in (Apollo TPS case) was used. Because of virtual ablation, the maximum TPS surface temperatures never exceeded 1,200°F. Toward the touchdown time (which varies with the reentry trajectory), the TPS surface temperatures for each heating case (figs. 29–30) became lower than the maximum temperature inside the TPS because the TPS surface experiences convective and radiation cooling during the latter part of the flight trajectory.

Composite Wall Temperatures

Figure 31 shows the TPS-side composite wall maximum temperatures (at touchdown) plotted

as functions of the TPS thickness, h, for the five heating cases with virtual ablation considered. Note that the substructural composite temperatures reached the composite operating limit temperature of 300°F at a TPS thicknesses of h = {0.767, 1.119, 1.538, 0.899, 1.211} inches respectively for the LR ballistic reentry, LR direct reentry, LR skipping reentry, LEO ballistic reentry, and LEO guided reentry.

Seen in figure 31, the lunar return ballistic heating case appears to be the most attractive reentry trajectory because it requires the minimum TPS thickness for protecting the GCEV, and therefore avoids excess TPS weight. The next attractive reentry trajectory is the low Earth orbit ballistic reentry case. The skipping reentry case performed poorly because it requires the thickest (heaviest) initial TPS for protecting the GCEV. Figure 31, together with table 6, provides a design tool for determining the stagnation point TPS thickness for a specified composite operating temperature under a specified reentry heating rate. The values for composite sandwich wall maximum temperatures, T_{SW}, at touchdown used in plotting figure 31 are listed in table 7 for the five lunar return reentry-heating rates.

Table 7. Composite sandwich wall maximum temperatures, T_{SW}, at touchdown based on different lunar return reentry heating cases.

h, in (TPS)	T_{SW}, °F				
	LR ballistic	LR direct	LR skipping	LEO ballistic	LEO guided
2.8 (Apollo)	70	71	99	70	72
2.6	70	72	112	70	74
2.4	70	74	131	70	77
2.2	70	78	155	71	84
2.0	71	86	187	73	97
1.8	72	102	228	77	120
1.6	77	130	281	87	158
1.538	-----	-----	300*	-----	-----
1.4	88	179	348	109	217
1.211	-----	-----	-----	-----	300*
1.2	115	258	433	153	306
1.119	-----	300*	-----	-----	-----
1.0	173	375	540	237	430
0.9	219	450	600	299	505
0.899	-----	-----	-----	300*	-----
0.8	278	535	-----	377	588
0.767	300*	-----	-----	-----	-----
0.7	352	-----	-----	473	-----
0.6	433	-----	-----	585	-----

* Limit operating temperature for graphite/epoxy composites.

THERMAL PROTECTION SYSTEM THICKNESSES AND WEIGHT REQUIREMENTS

Once the maximum recession depth (table 6) and the ablated minimum TPS thicknesses (table 7) are determined, the allowable minimum initial TPS thicknesses may be obtained by summing up the above two components. The corresponding initial TPS weights may be calculated from equation (14) using the values of the initial minimum TPS thicknesses. The results are summarized in table 8 for the five heating cases.

Table 8. Initial minimum TPS thicknesses and the associated TPS weights.

	Reentry heating	δ_{max}, in (a)	h_V, in (b)	$h_{min} = \delta_{max} + h_V$ in (a)+(b)	Initial TPS weight, W, lb	Weight ratio
(1)	LR abort ballistic reentry	0.55	0.767	1.317	816	1.00‡
(2)	LR guided direct reentry	0.91	1.119	2.029	1,258	1.54
(3)	LR guided skipping reentry	0.83	1.538	2.368	1,468*	1.80
(4)	LEO abort ballistic reentry	0.28	0.899	1.179	731†	0.90
(5)	LEO nominal guided reentry	0.37	1.211	1.581	980	1.20

* Heaviest

† Lightest

‡ Weight ratio basis

Table 8 shows that of the three lunar reentries, the LR abort ballistic reentry (1) requires much less TPS to keep the composite sandwich wall at the maximum allowable temperature, 300ºF than the LR guided direct reentry (2) or LR guided skipping reentry (3). As might be expected, one of the low Earth orbit reentries [LEO abort ballistic (4)] required the least TPS to protect the substructure. It is somewhat surprising, however, that for the two LEO reentries [(4) and (5)], which would be expected to require considerably less TPS than the three LR reentries [(1), (2), (3)], the LEO nominal guided reentry (5) actually required 20 percent more TPS weight, and the LEO abort ballistic reentry (4) required only 10 percent less TPS weight, than the LR abort ballistic reentry (1). These results indicate that based on the present analysis and using the weight of the TPS as the only criteria, the LR abort ballistic reentry (1) would be the trajectory of choice because the weight penalty required to obtain the low Earth orbit will probably be greater than the 10 percent difference in TPS weight.

SUMMARY

Thermostructural analysis was performed on windward wall structures of a generic CEV subjected to five cases of candidate reentry heating. Three of the reentry profiles were lunar return reentries and two of the reentry profiles were low Earth orbit reentries. The three lunar return reentries were (1) abort ballistic reentry, (2) guided direct reentry, and (3) guided skipping reentry. The two low Earth orbit reentries were (4) abort ballistic reentry and (5) nominal guided reentry. The results of this investigation led to the following conclusions.

1. To keep the substructure at 300ºF, the LR guided direct reentry, the LR guided skipping reentry, and the LEO nominal guided reentry required 54 percent more, 80 percent more, and 20 percent more TPS weight respectively than the LR abort ballistic reentry.
2. The LEO abort ballistic reentry required the lowest TPS weight to maintain the substructure at 300ºF. This TPS weight, however, was only 10 percent less than the TPS weight required for the LR abort ballistic reentry, and this weight difference is likely less than the weight penalty imposed to obtain the low Earth orbit.
3. The LR guided skipping reentry required almost twice as much TPS as the LR abort ballistic reentry, and required the most (heaviest) TPS of all reentry profiles analyzed.
4. A virtual ablation method (graphical approximation) developed earlier was further extended for more accurate estimations of ablation periods, ablation heat loads, and TPS recession layer thicknesses.
5. For the five heating cases {1, 2, 3, 4, 5}, up to {96, 93, 88, 86, 82} percent of the respective total reentry heat loads were consumed in the TPS ablation process, leaving small remaining amounts {3, 6, 8, 11, 15} percent of the respective total reentry heat loads to heat and maintain the TPS surface temperature at 1,200ºF during ablation periods.
6. For the five heating cases {1, 2, 3, 4, 5}, the virtual ablation periods lasted for {138, 476, 654, 276, 531} sec respectively
7. For the five heating cases {1, 2, 3, 4, 5}, the estimated stagnation point TPS recession layer depths were estimated to be {0.55, 0.91, 0.83, 0.28, 0.37} inches respectively.
8. For the five heating cases {1, 2, 3, 4, 5}, the stagnation point TPS thicknesses of {0.767, 1.119, 1.538, 0.899, 1.211} inches were found to be the respective minimum allowable thicknesses to maintain the substructural composite sandwich temperature at the limit of 300°F.

FIGURES

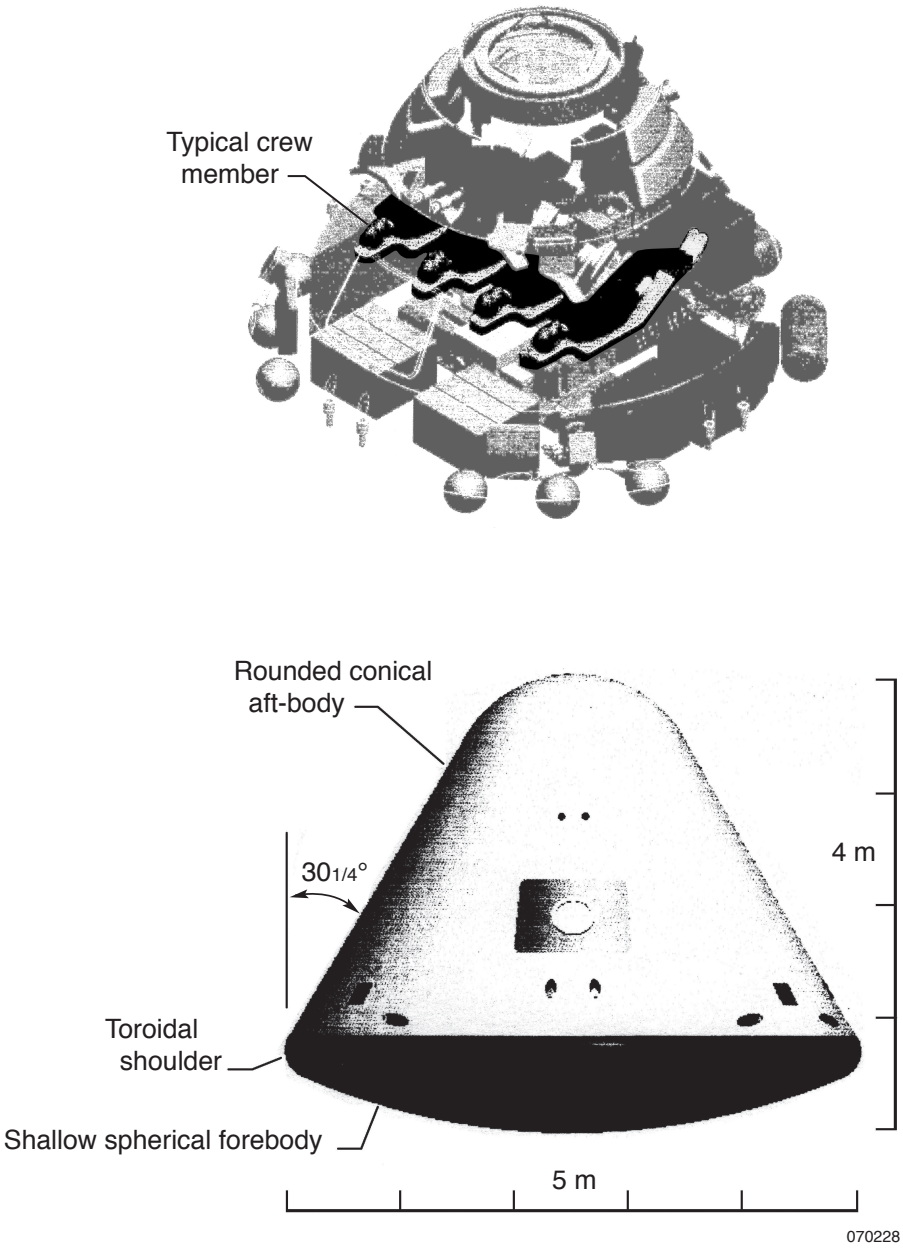

Figure 1. Geometry of a candidate CEV (crew exploration vehicle).

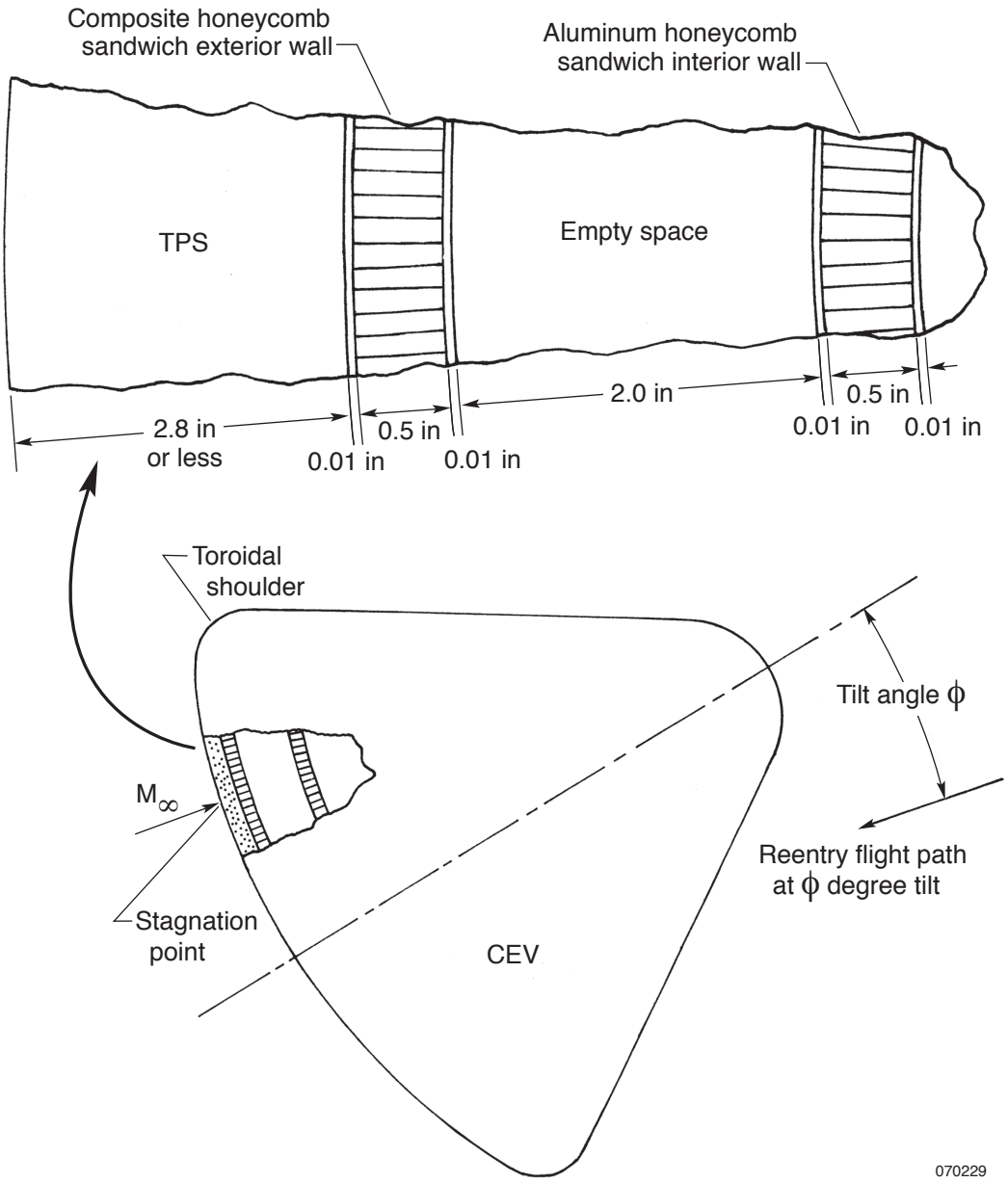

Figure 2. Geometry of a generic CEV with dual sandwich walls.

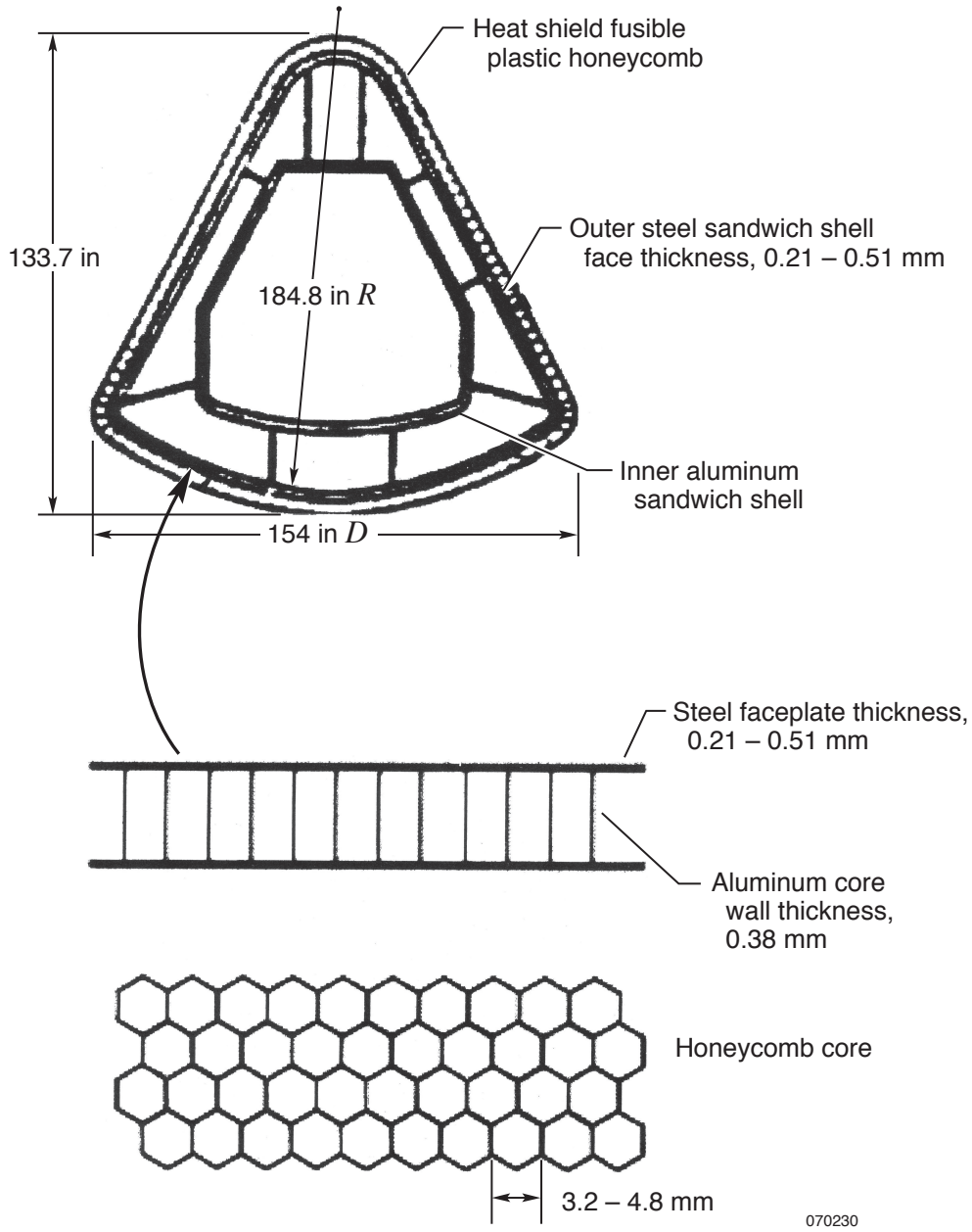

Figure 3. Double-walled sandwich construction of the Apollo capsule.

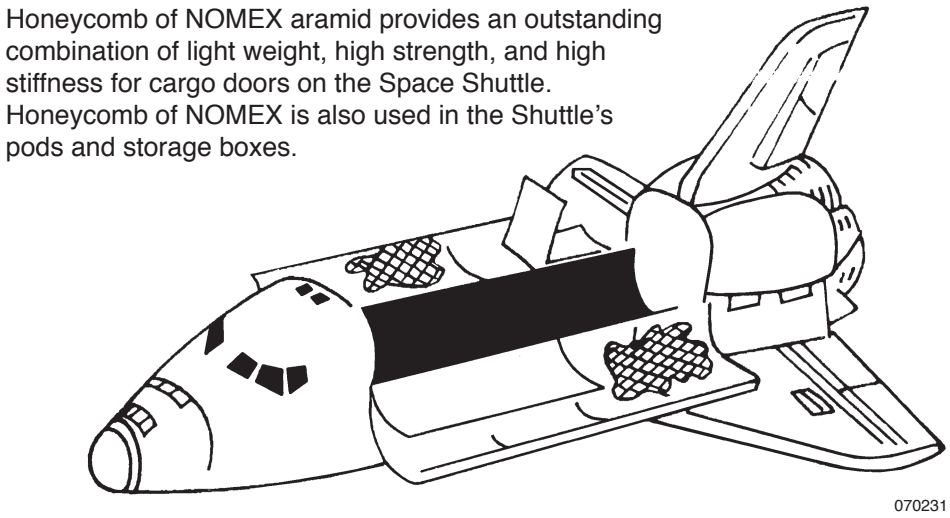

Figure 4. Space Shuttle Orbiter cargo bay doors (graphite-epoxy face sheets/NOMEX honeycomb core sandwich construction).

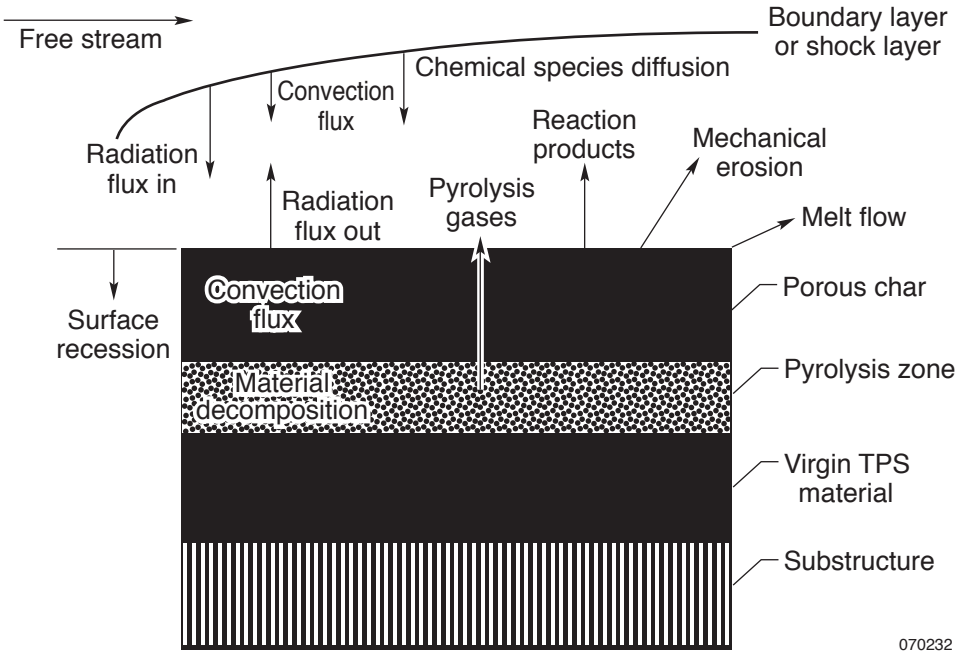

Figure 5. Energy accommodation mechanisms of ablative TPS material (ref. 5).

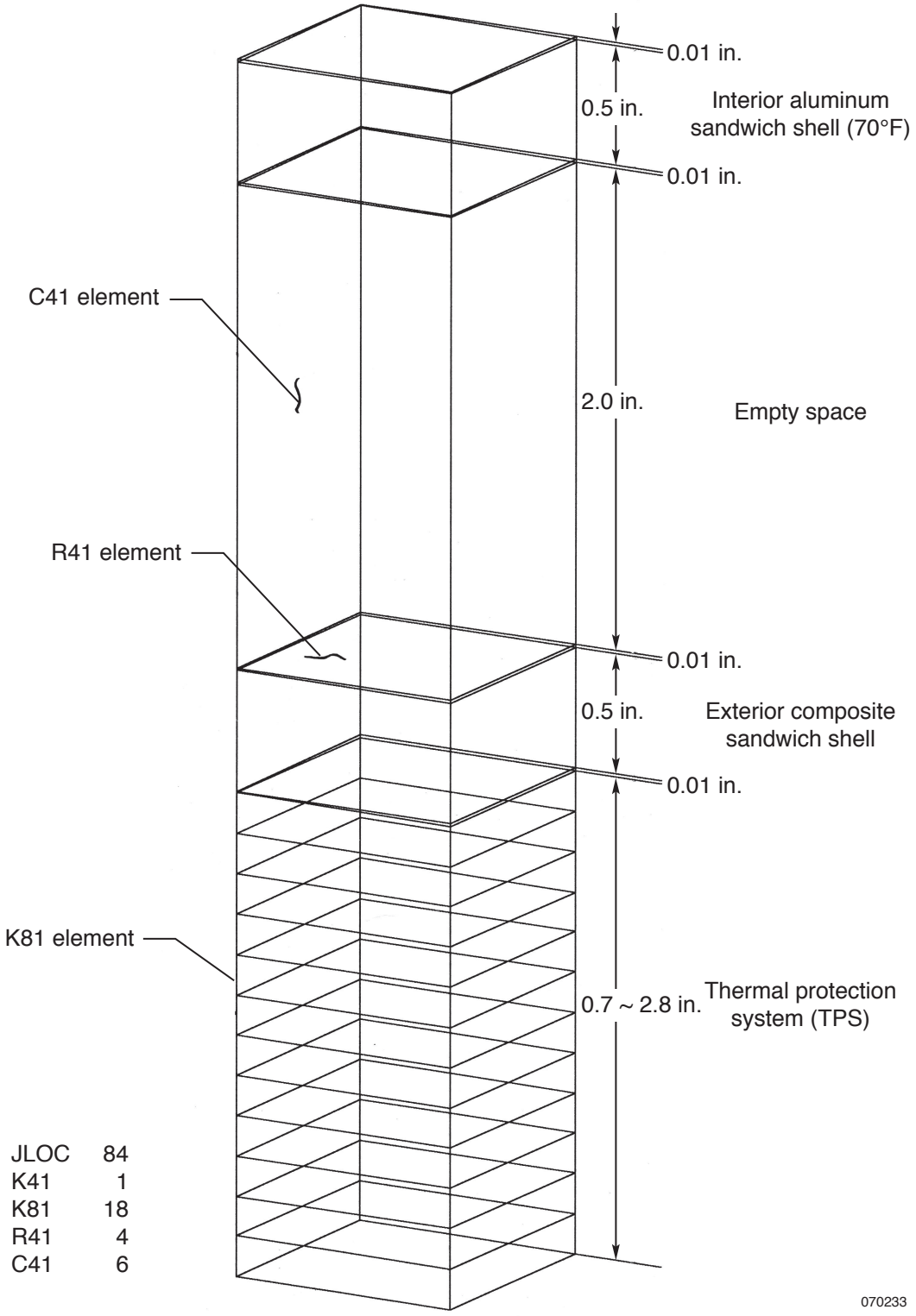

Figure 6. Simple-plug thermal model generated for GCEV windward wall.

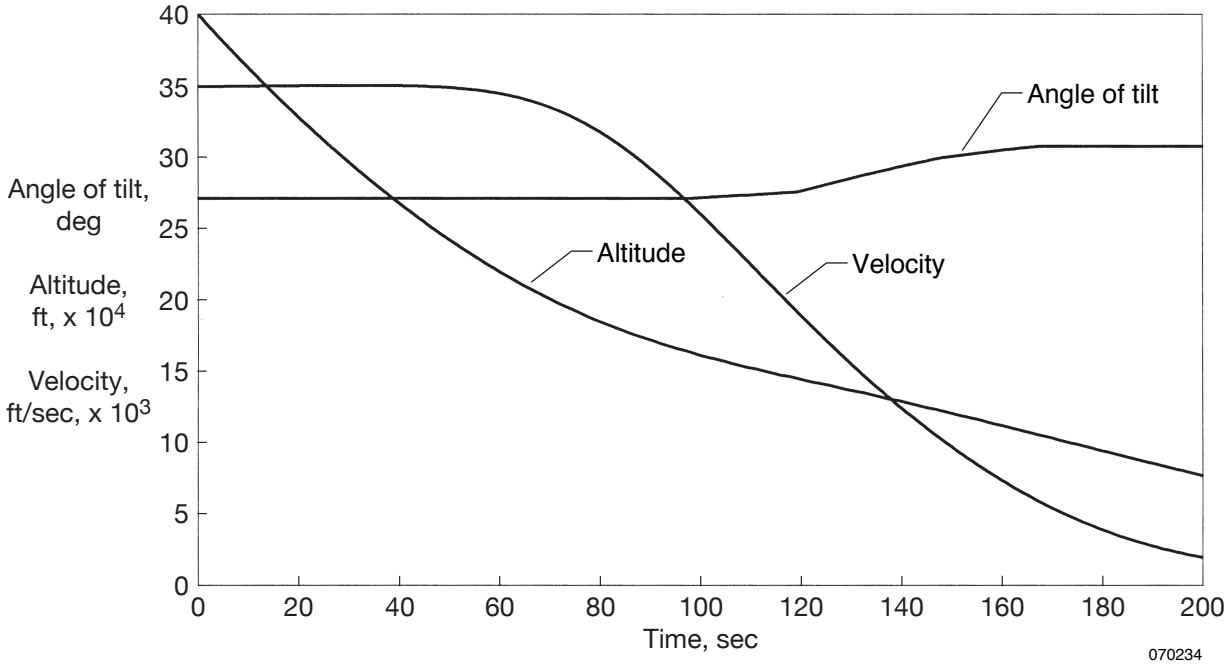

Figure 7. Crew exploration vehicle lunar return abort ballistic reentry trajectories.

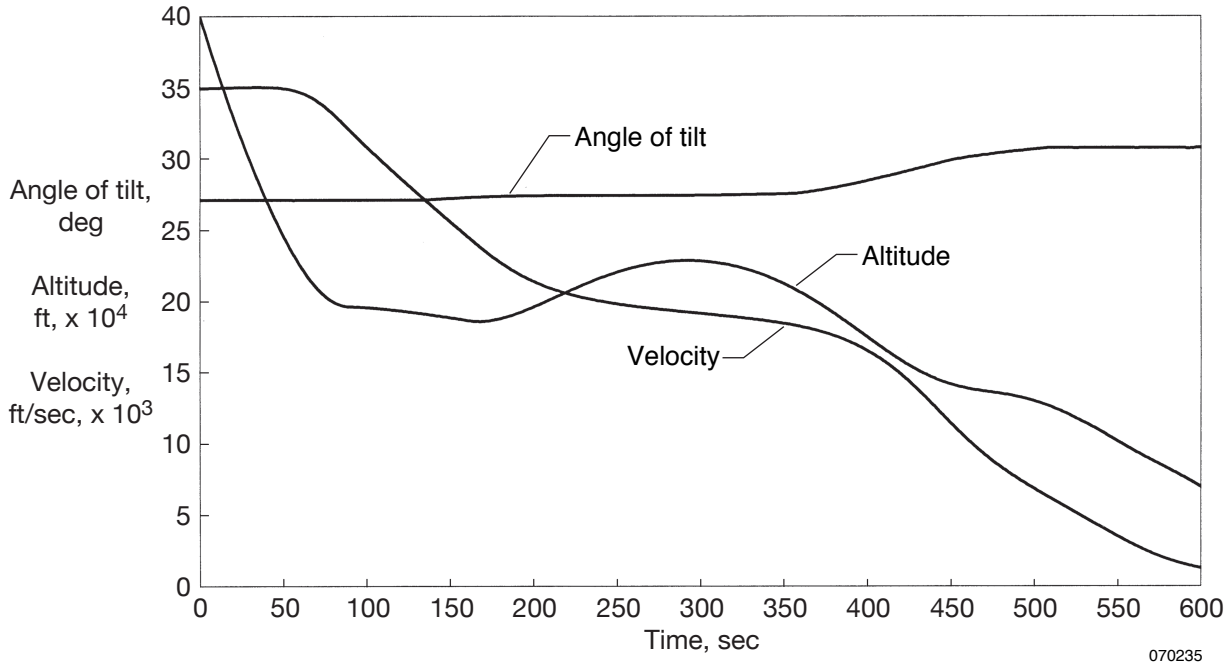

Figure 8. Crew exploration vehicle lunar return guided direct reentry trajectories.

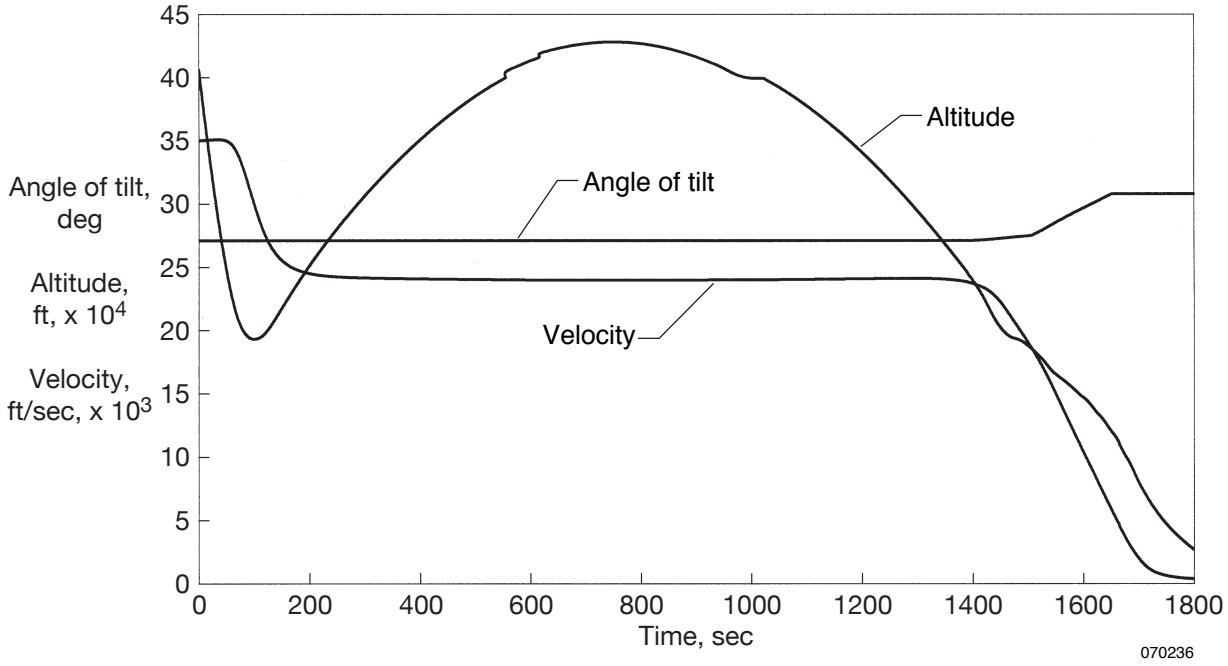

Figure 9. Crew exploration vehicle lunar return guided skipping reentry trajectories.

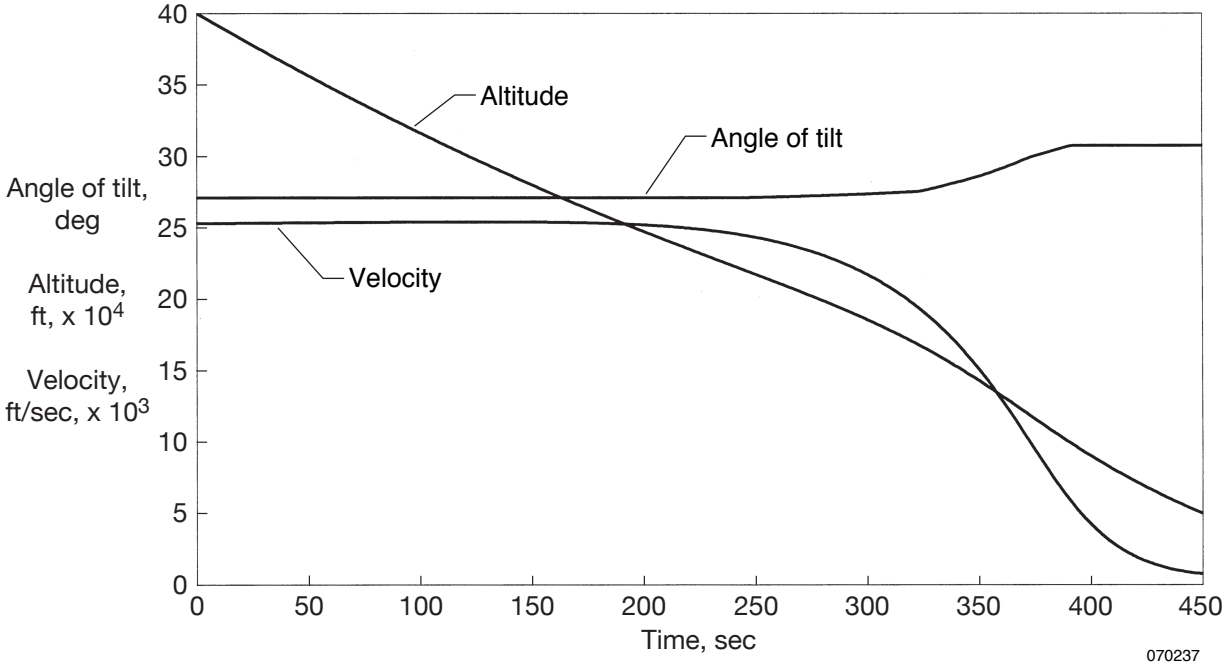

Figure 10. Crew exploration vehicle low Earth orbit abort ballistic reentry trajectories.

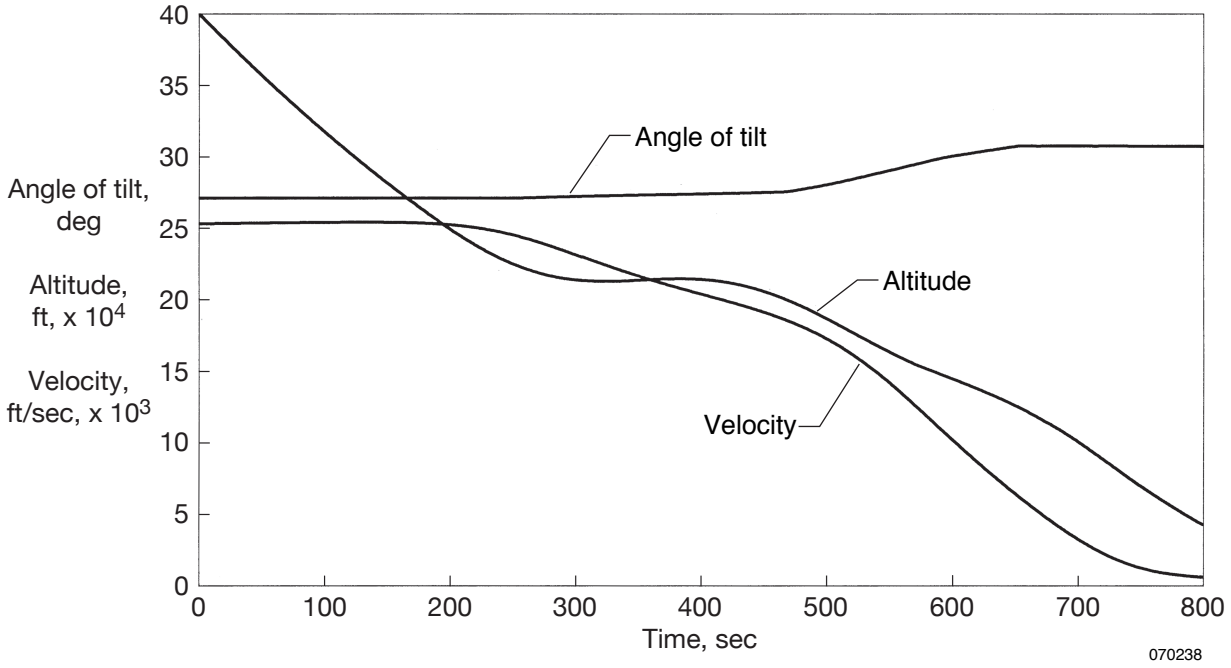

Figure 11. Crew exploration vehicle low Earth orbit nominal guided reentry trajectories.

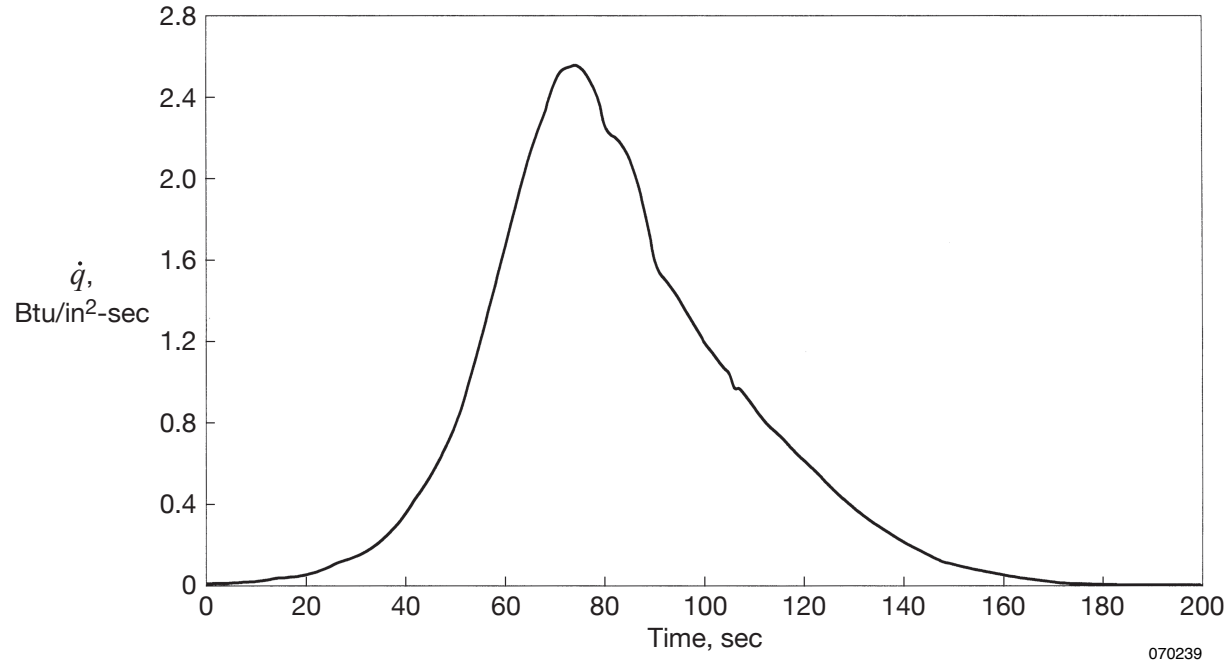

Figure 12. Crew exploration vehicle stagnation point heating rate time history; lunar return abort ballistic reentry.

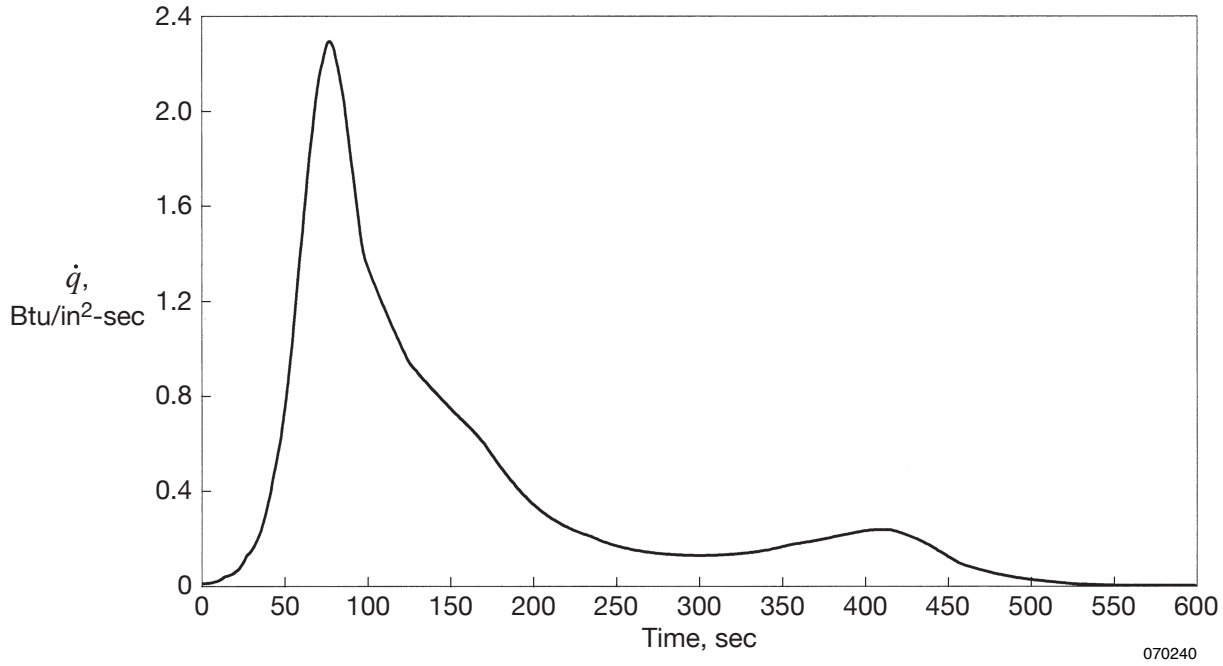

Figure 13. Crew exploration vehicle stagnation point heating rate time history; lunar return guided direct reentry.

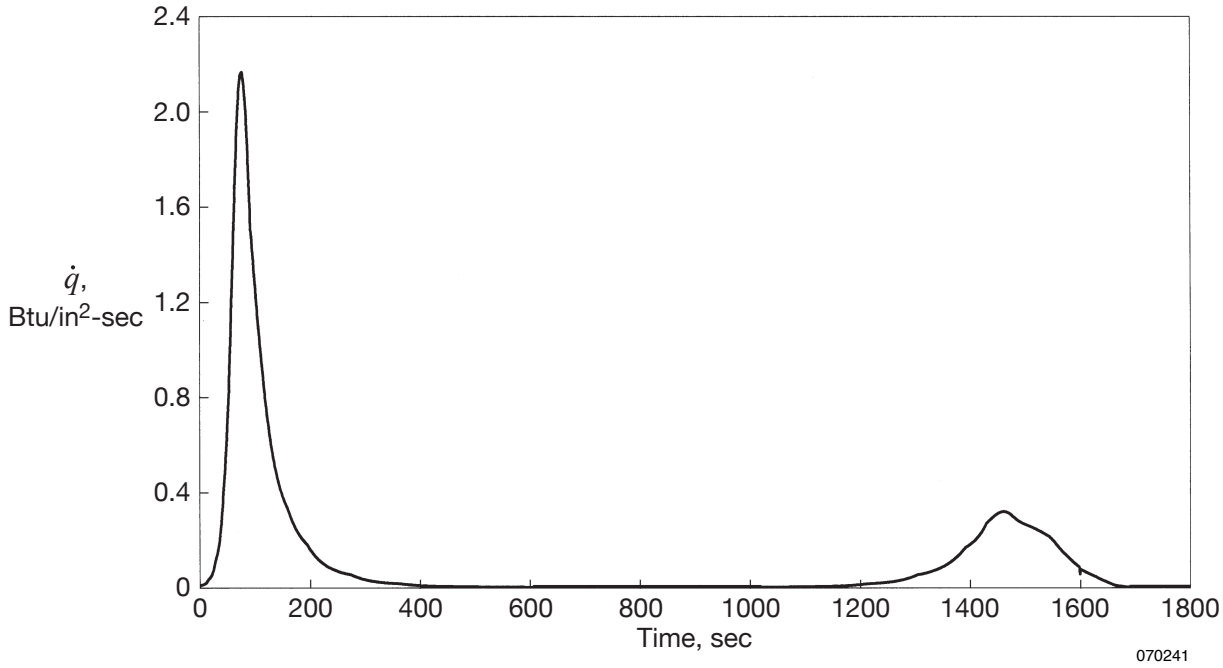

Figure 14. Crew exploration vehicle stagnation point heating rate time history; lunar return guided skipping reentry.

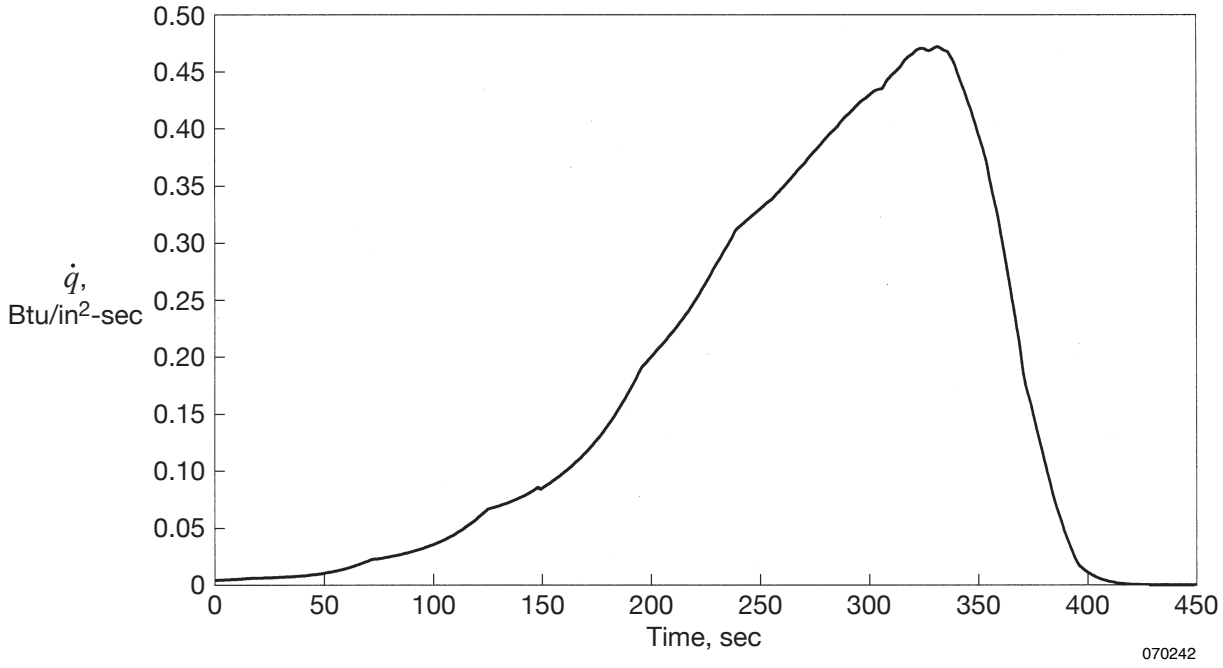

Figure 15. Crew exploration vehicle stagnation point heating rate time history; low Earth orbit abort ballistic reentry.

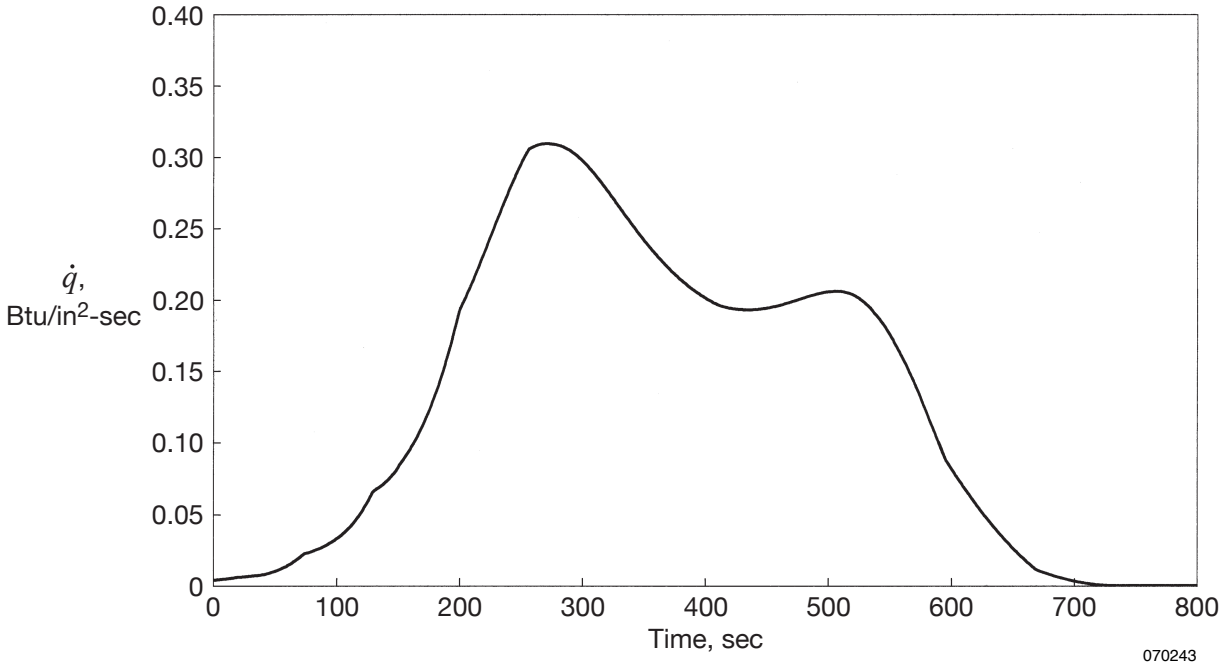

Figure 16. Crew exploration vehicle stagnation point heating rate time history low Earth orbit nominal guided reentry.

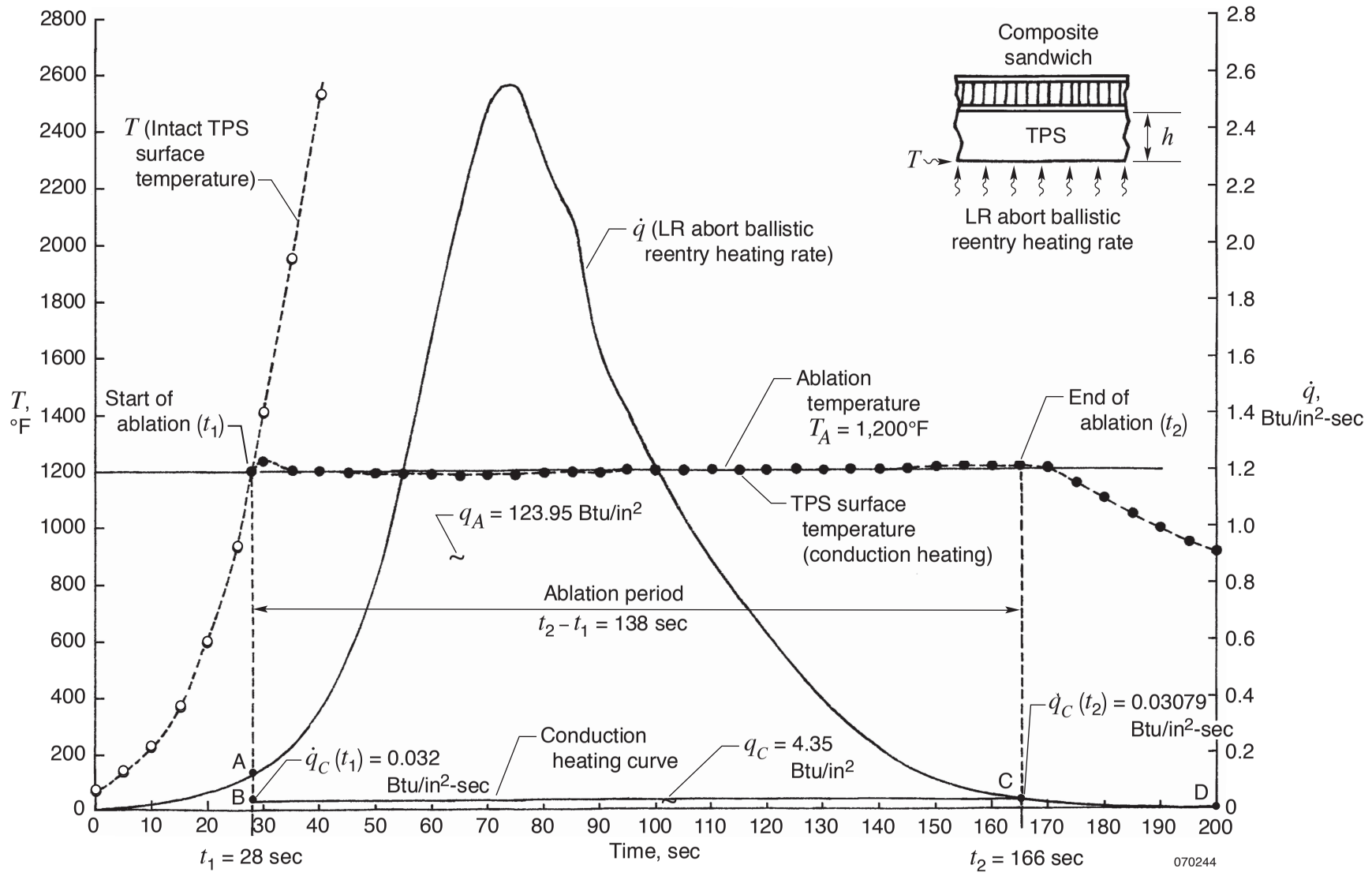

Figure 17. Heating curve and associated TPS surface temperature curves for graphical virtual ablation analysis; lunar return abort ballistic reentry.

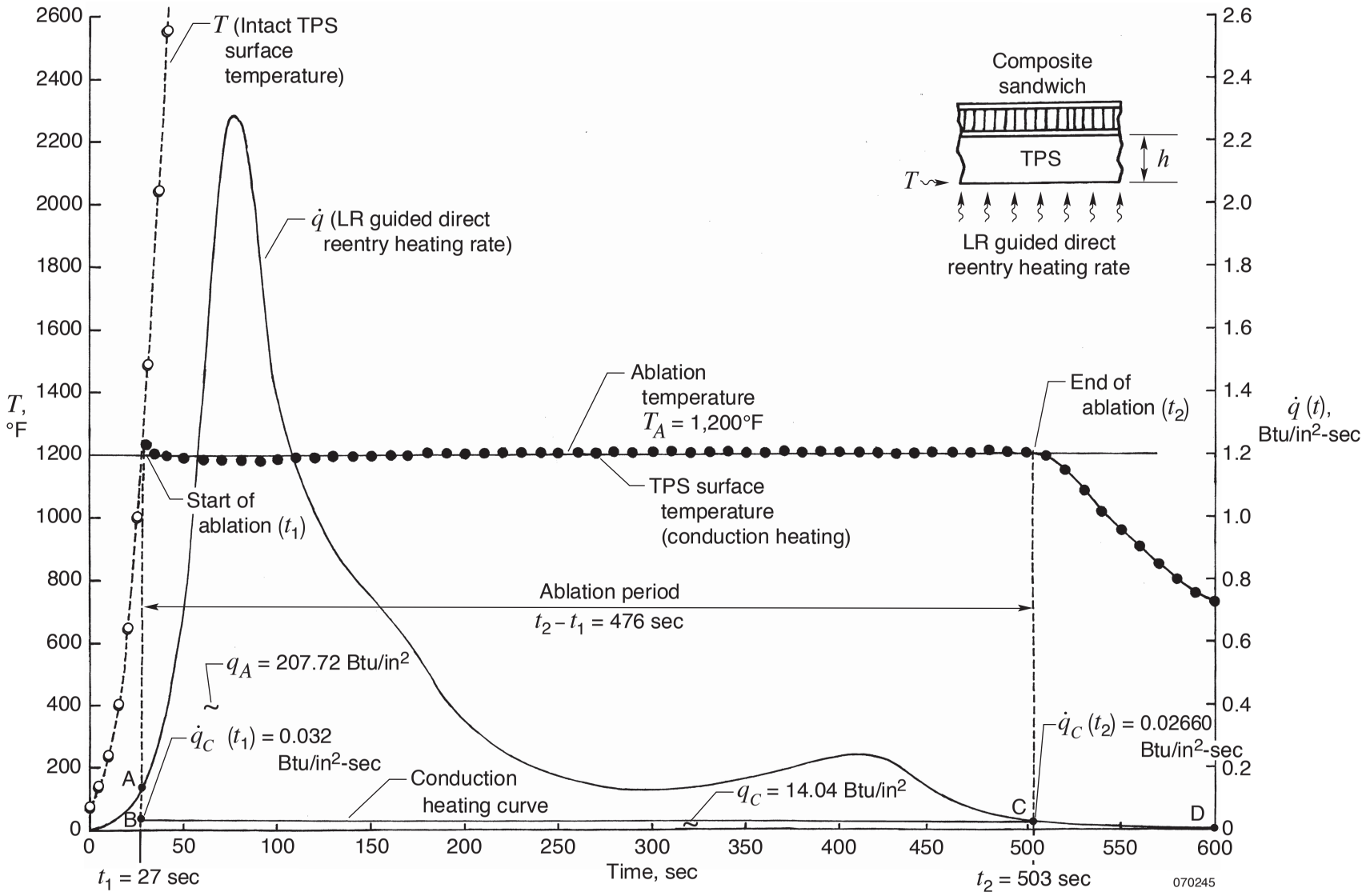

Figure 18. Heating curve and associated TPS surface temperature curves for graphical virtual ablation analysis; lunar return guided direct reentry.

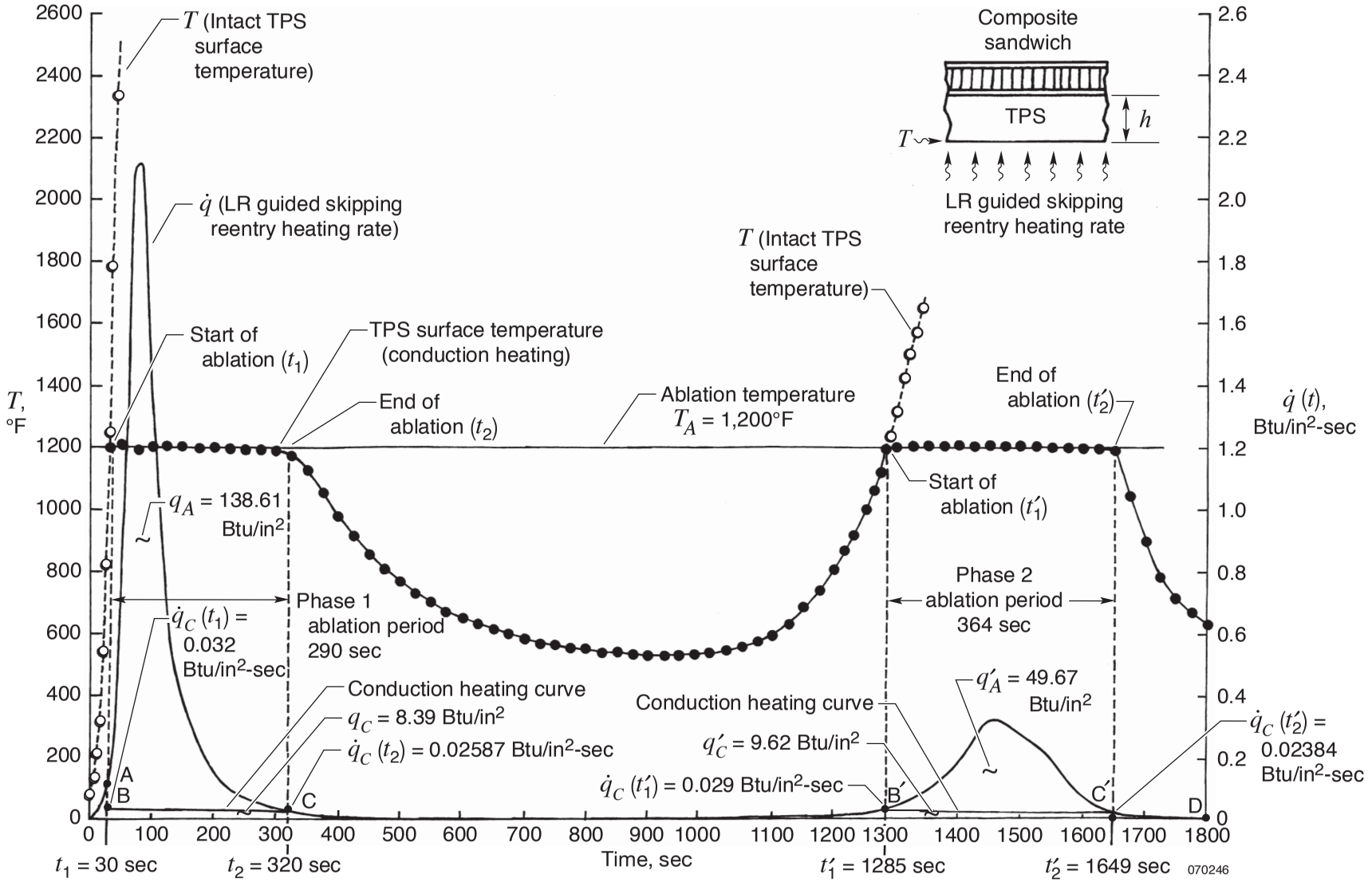

Figure 19. Heating curve and associated TPS surface temperature curves for graphical virtual ablation analysis; lunar return guided skipping reentry.

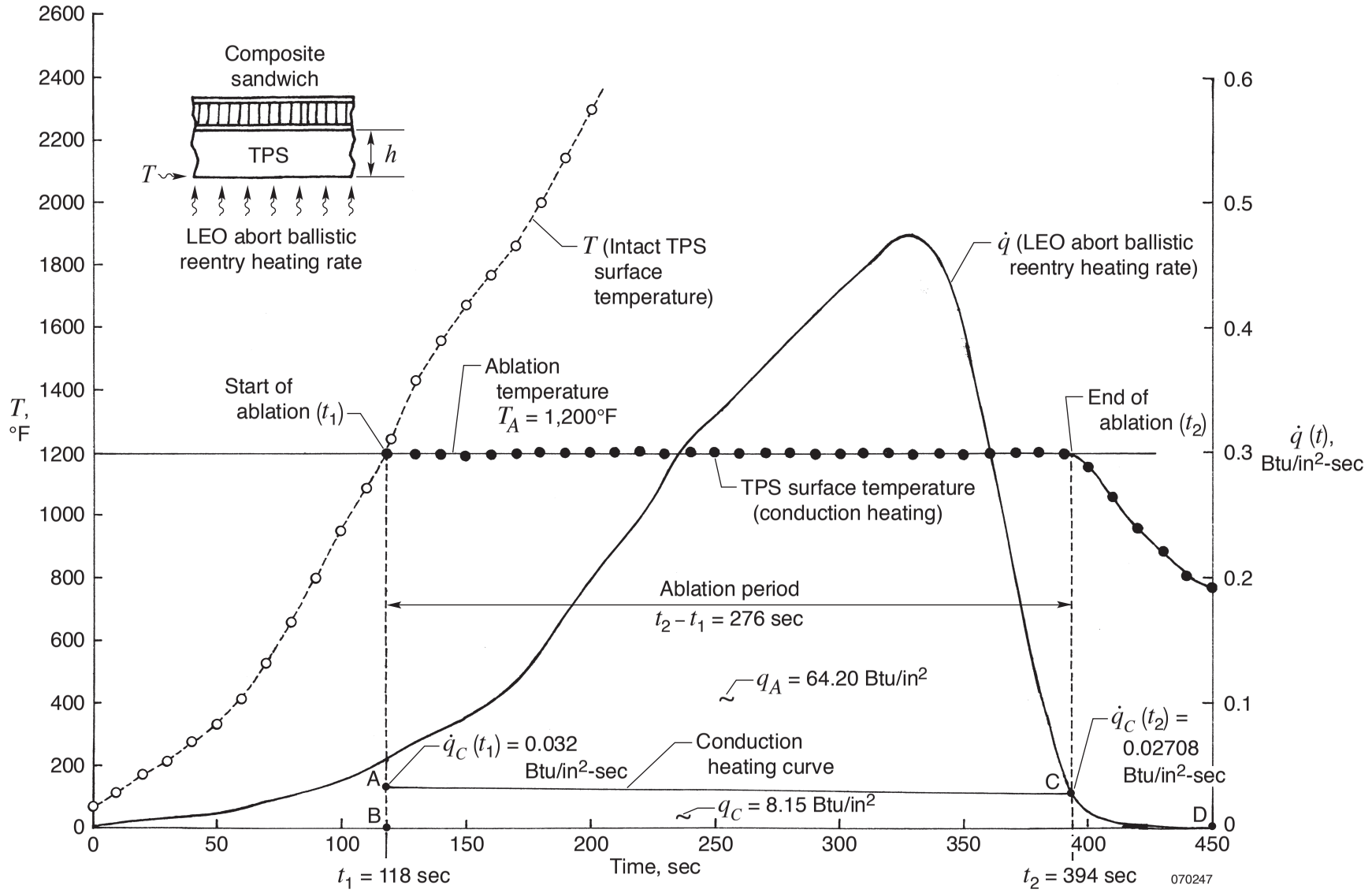

Figure 20. Heating curve and associated TPS surface temperature curves for graphical virtual ablation analysis, low Earth orbit abort ballistic reentry.

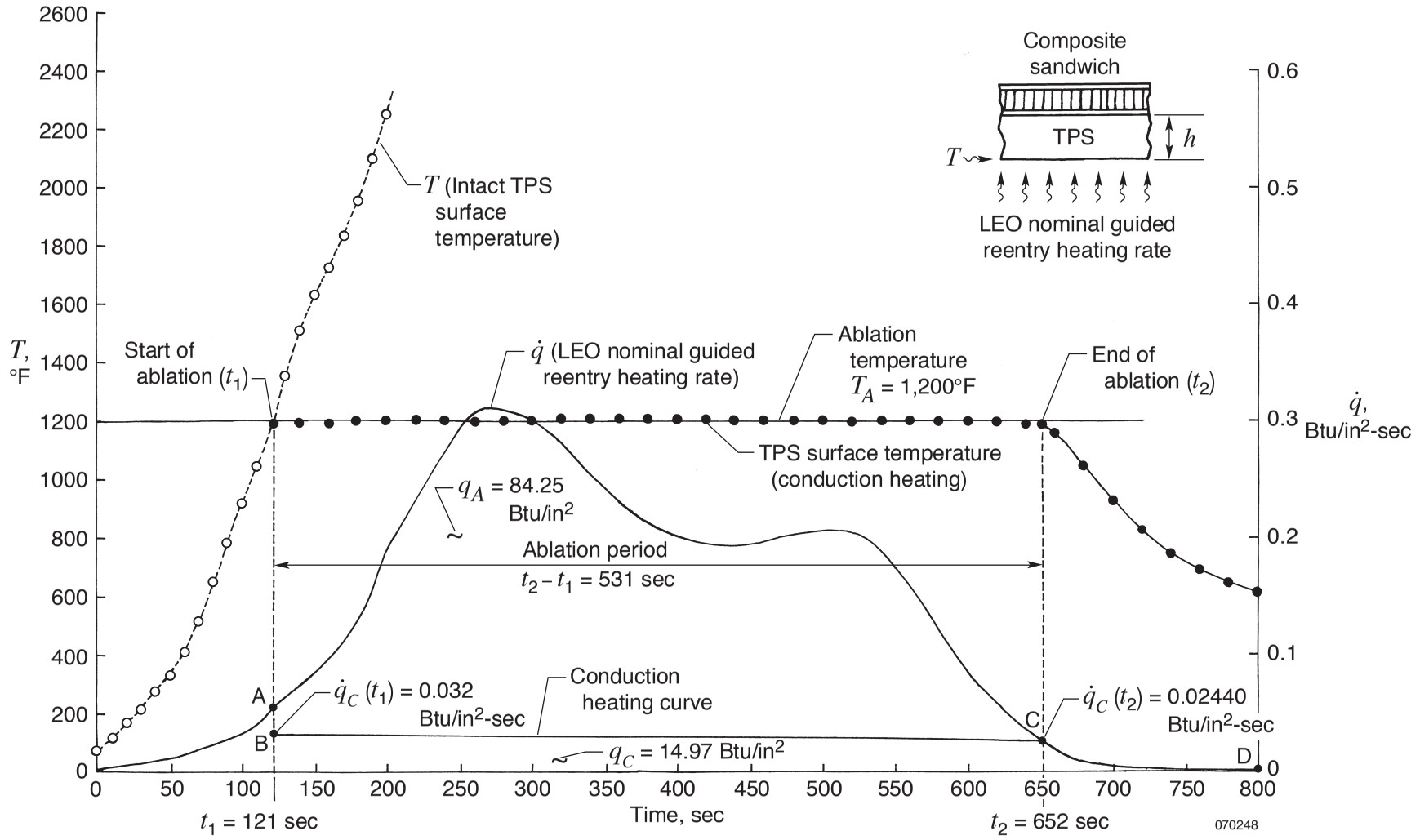

Figure 21. Heating curve and associated TPS surface temperature curves for graphical virtual ablation analysis, low Earth orbit nominal guided reentry.

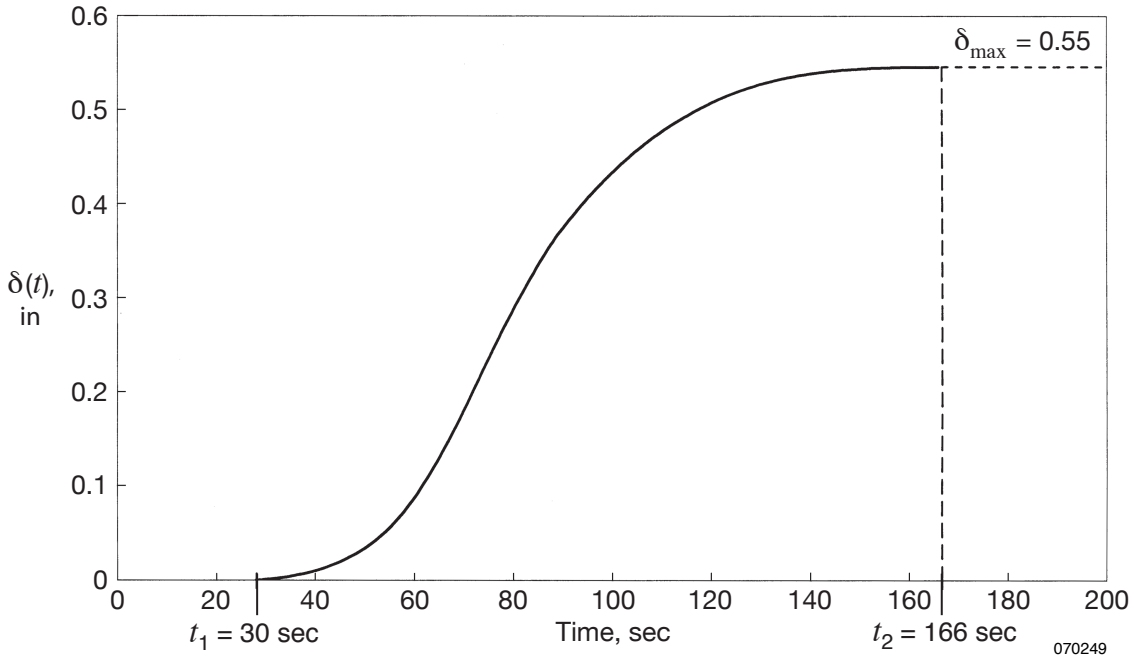

Figure 22. Thermal protection system recession layer thickness, $\delta(t)$, plotted as a function of time; lunar return abort ballistic reentry.

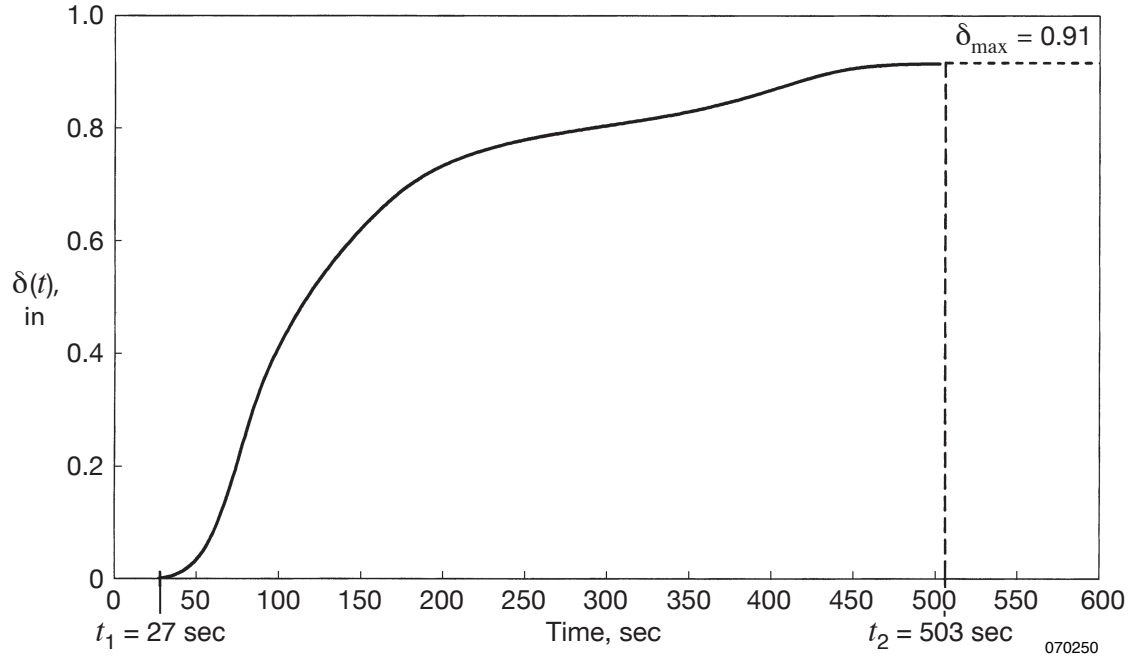

Figure 23. Thermal protection system recession layer thickness, $\delta(t)$, plotted as a function of time; lunar return guided direct reentry.

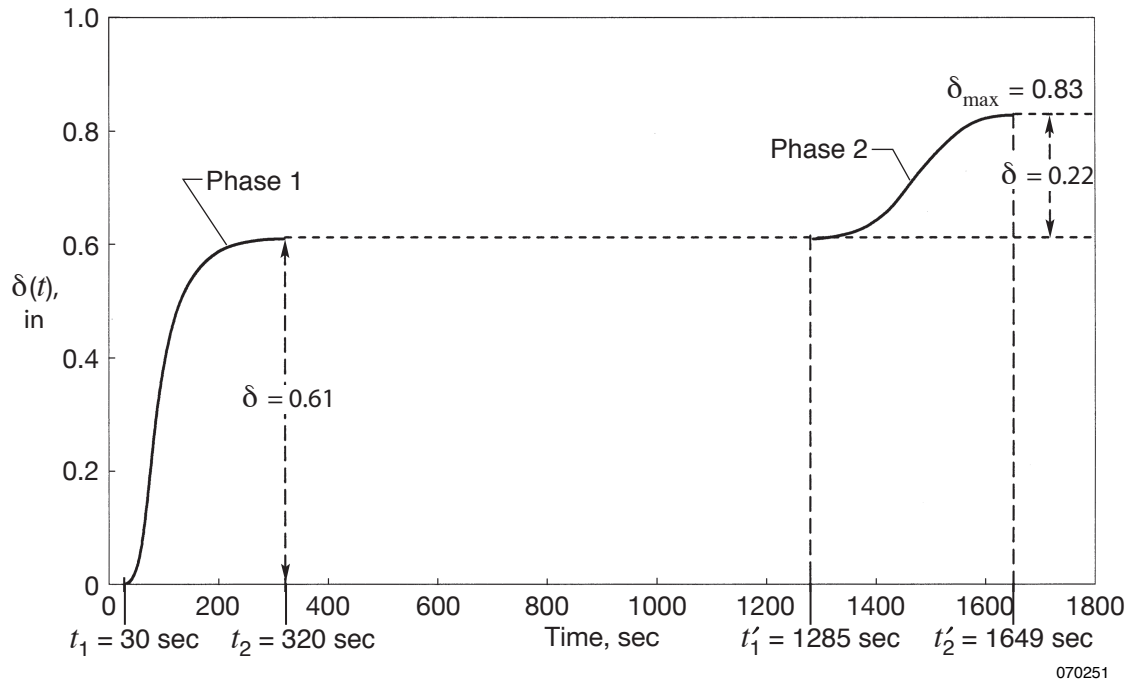

Figure 24. Thermal protection system recession layer thickness, $\delta(t)$, plotted as a function of time; lunar return guided skipping reentry.

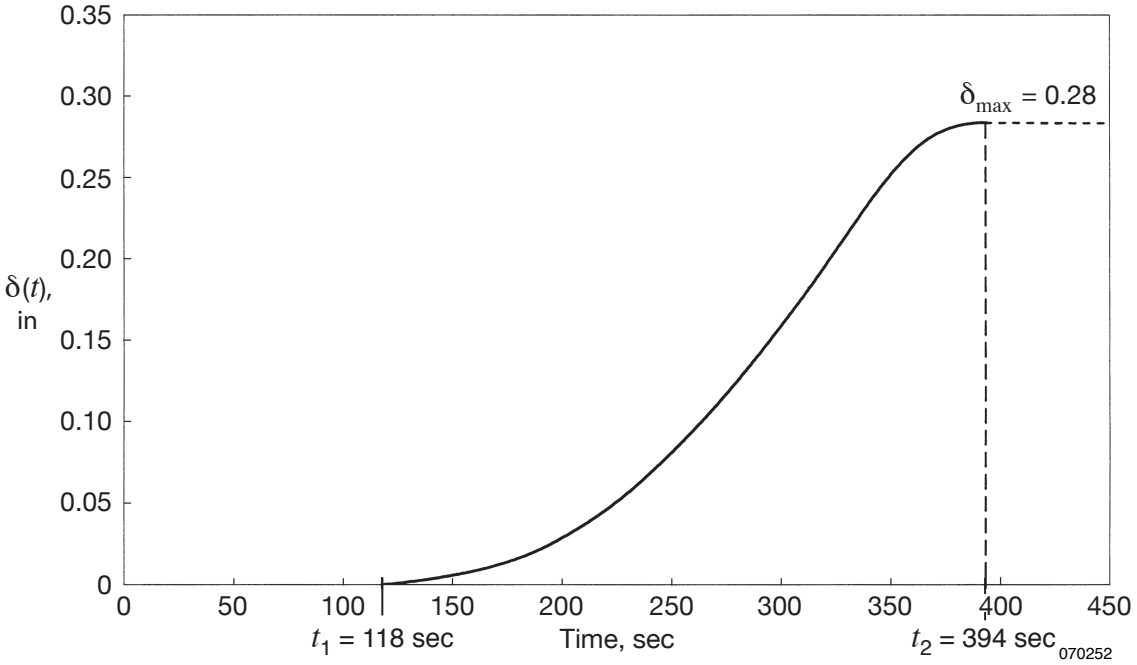

Figure 25. Thermal protection system recession layer thickness, $\delta(t)$, plotted as a function of time; low Earth orbit abort ballistic reentry.

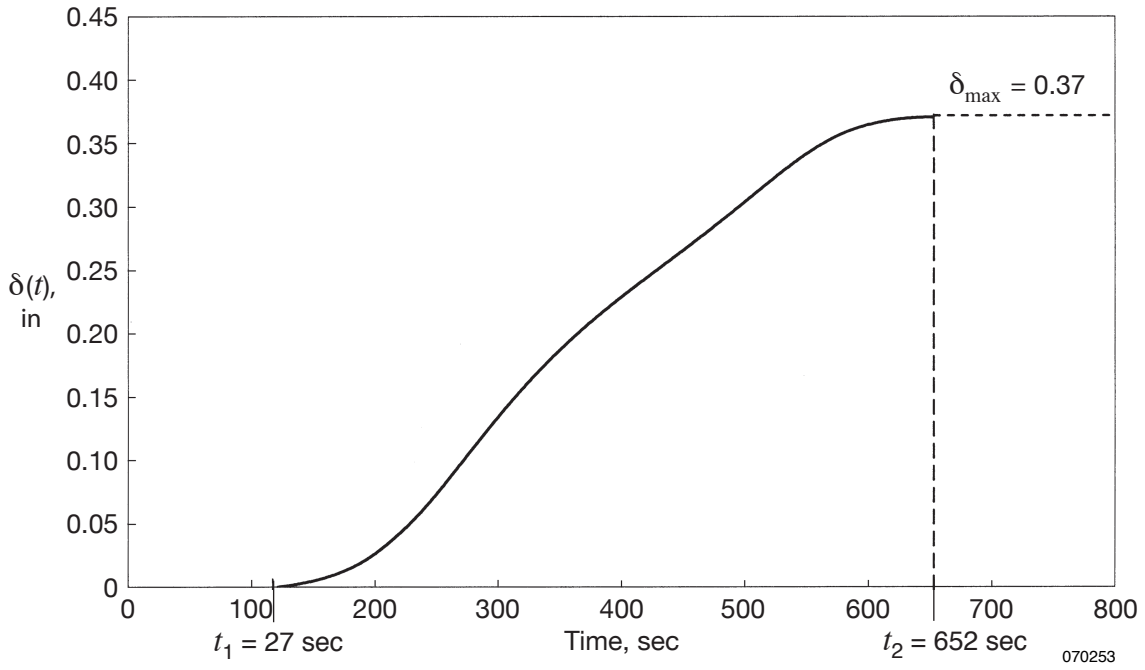

Figure 26. Thermal protection system recession layer thickness, $\delta(t)$, plotted as a function of time; low Earth orbit nominal guided reentry.

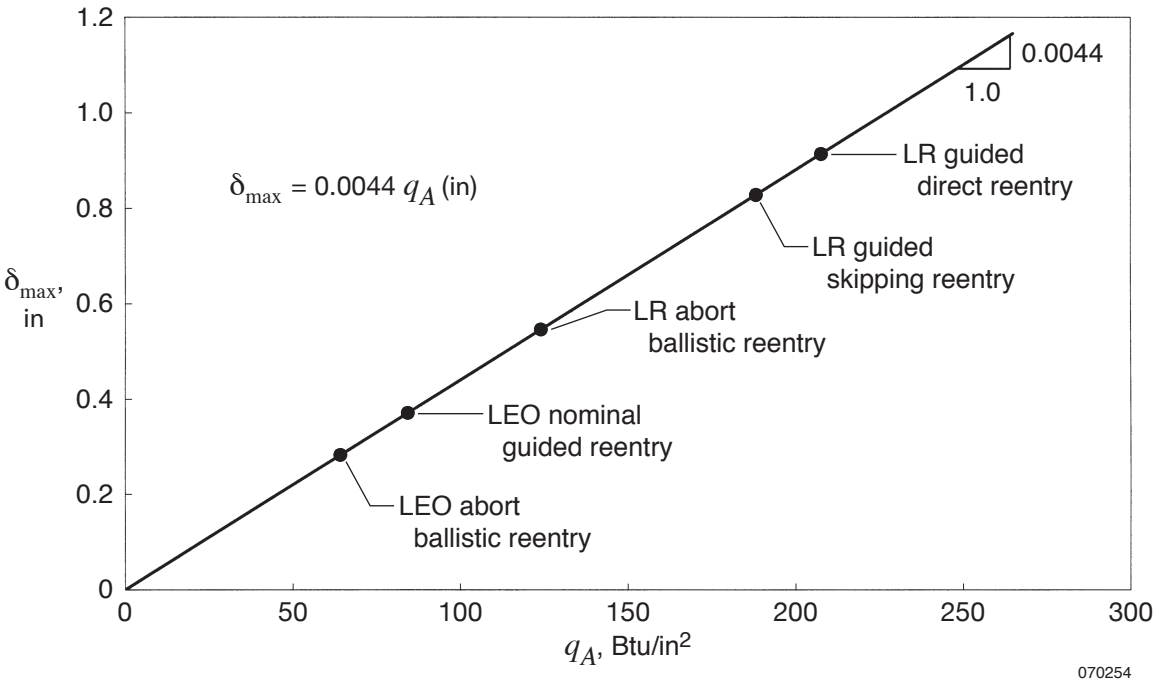

Figure 27. Maximum thermal protection system recession layer thickness, δ_{max}, plotted as a function of ablation heat load, q_A.

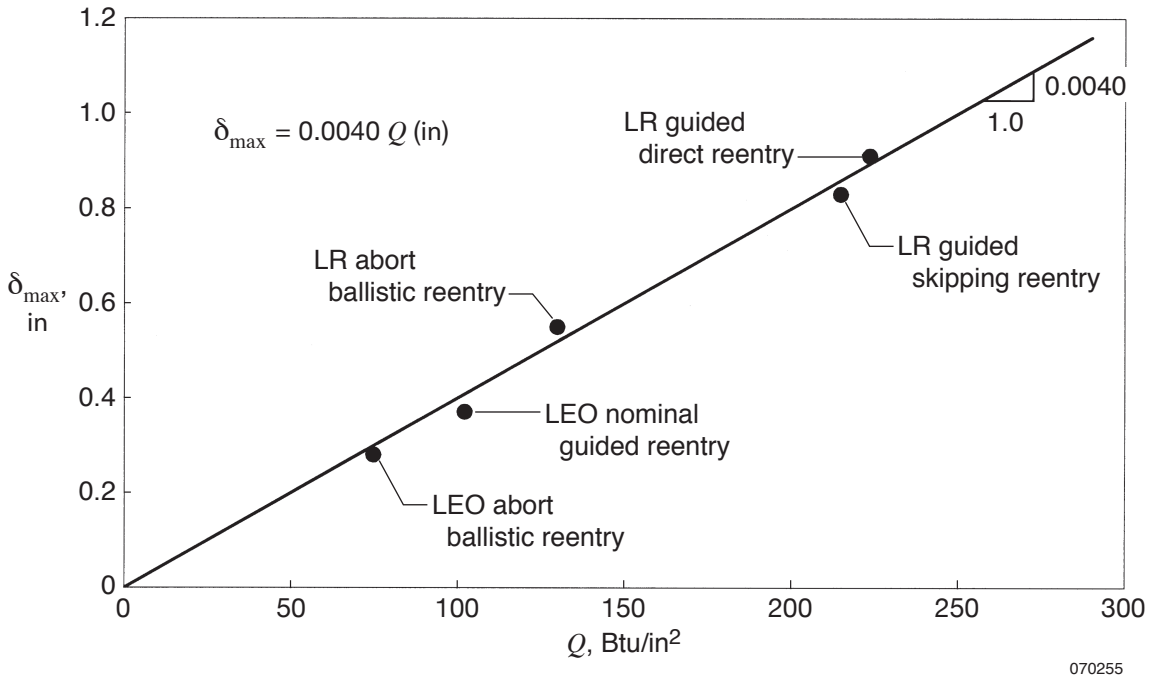

Figure 28. Maximum thermal protection system recession layer thickness, δ_{max}, plotted as a function of total reentry heat load, Q.

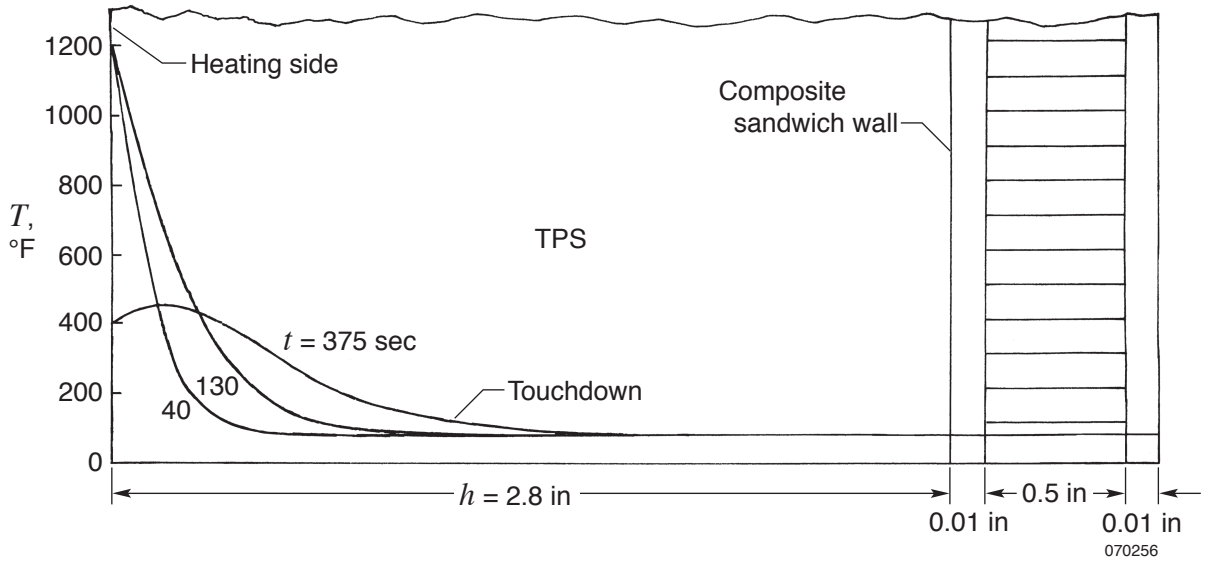

(a) Lunar return abort ballistic reentry.

Figure 29. Temperature distributions across the GCEV stagnation point wall at different time steps; lunar return reentry heating rates; h = 2.8 in (Apollo TPS thickness).

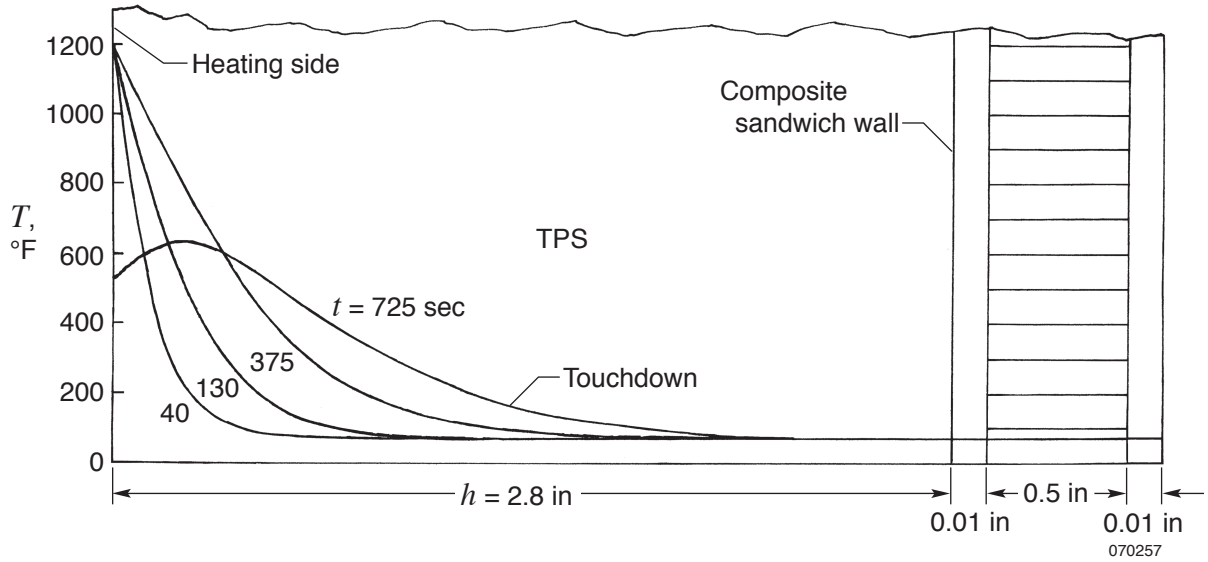

(b) Lunar return guided direct reentry.

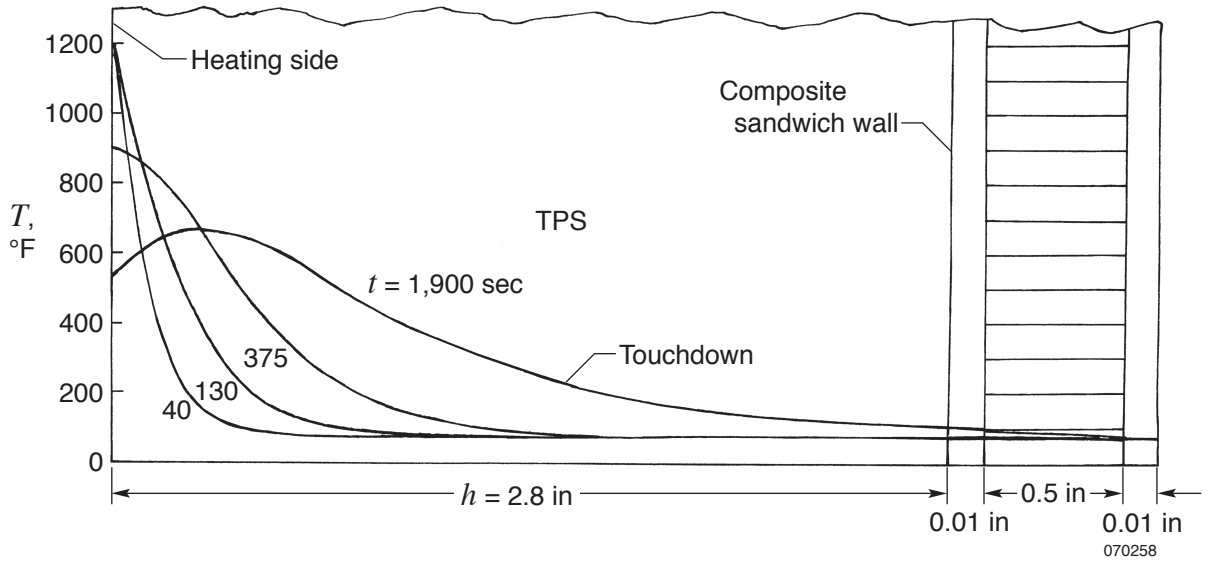

(c) Lunar return guided skipping reentry.

Figure 29. Concluded.

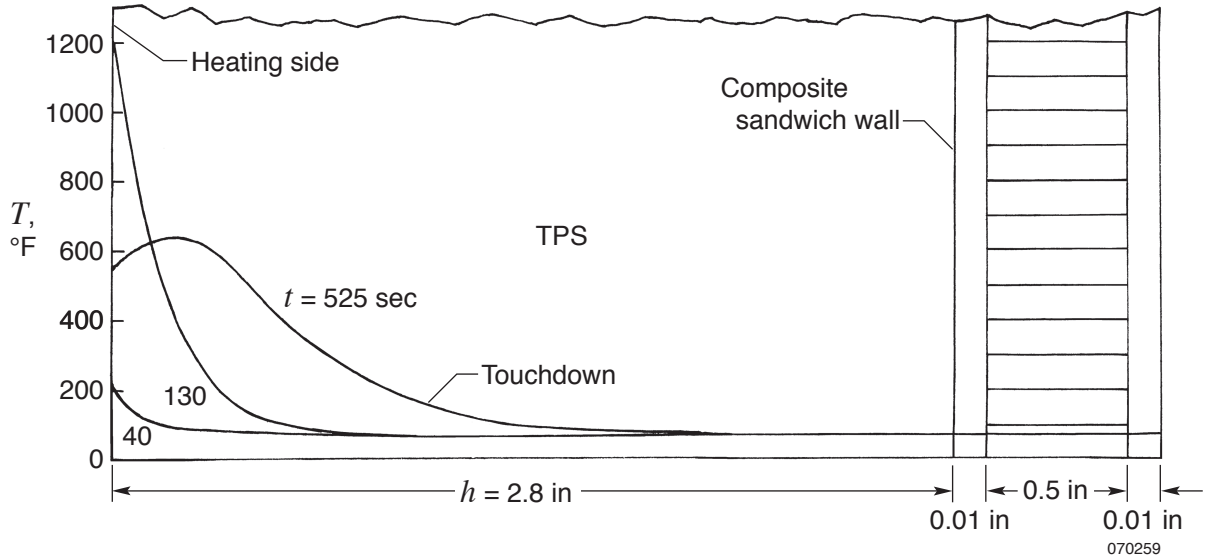

(a) Low Earth orbit abort ballistic reentry.

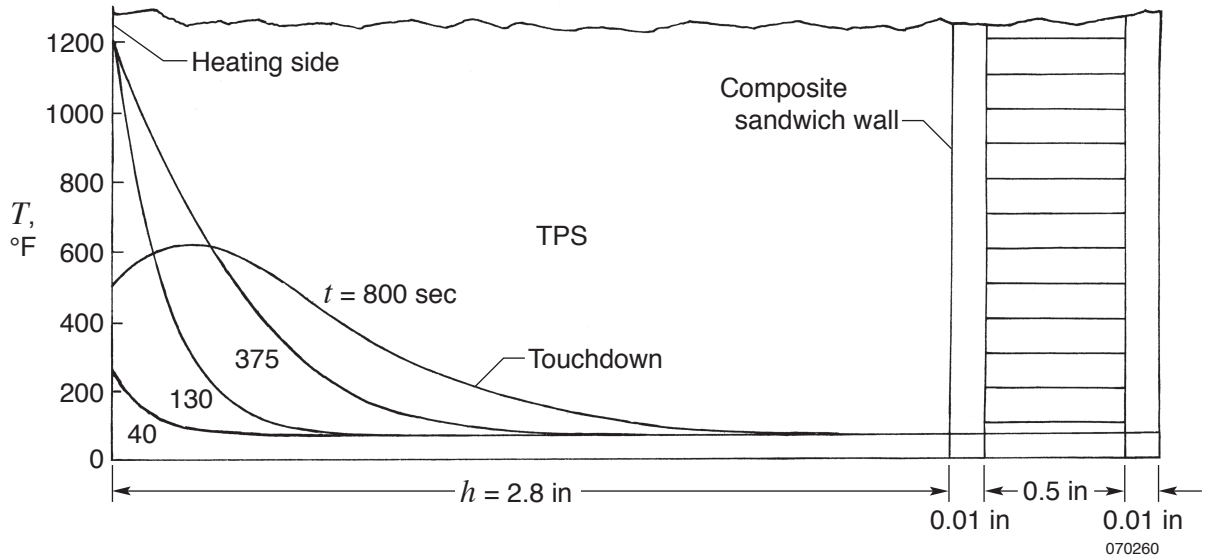

(b) Low Earth orbit nominal guided reentry.

Figure 30. Temperature distributions across the GCEV stagnation point wall at different time steps; low Earth orbit reentry heating rates; h = 2.8 in (Apollo TPS thickness).

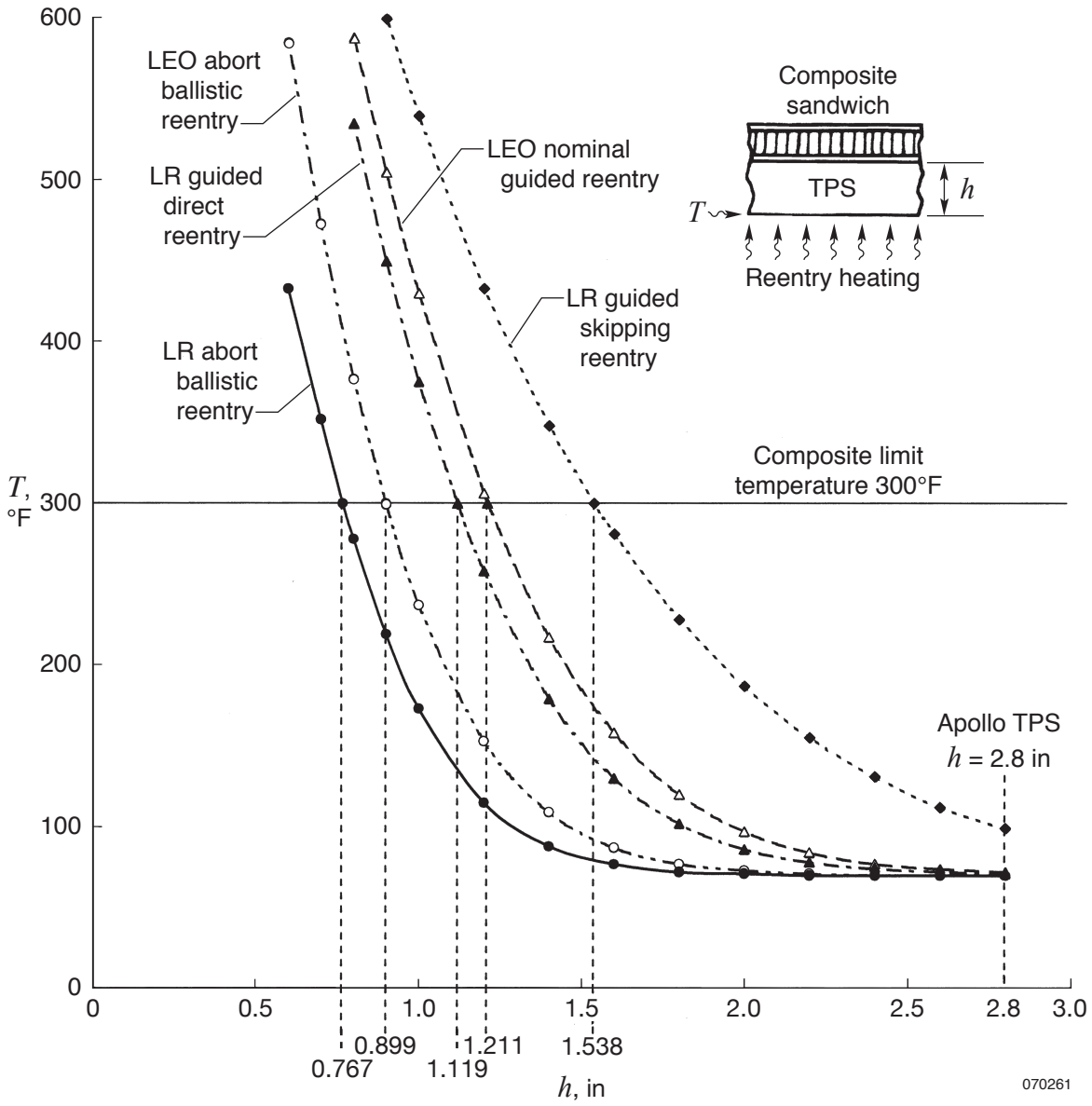

Figure 31. Maximum composite substructural temperatures at touchdown plotted as functions of TPS thickness, *h*, for different reentry heating cases.

APPENDIX A
REFERENCE SPACE VEHICLES

The Apollo Capsule

Figure 3 shows the structure of the Apollo capsule, a double-walled construction. The windward curved circular shell has a 154.0 in diameter and 184.8 in radius of curvature. The fairing between the spherical segment and the conical segment are connected by a toroidal shoulder with a 7.7 in radius. The aft-body is a circular cone with sidewall angle of 33 deg measured from the axis of symmetry. The capsule outer shell [immediately beneath the thermal protection system (TPS)] is a sandwich shell fabricated with aluminum honeycomb core with steel face sheets at both sides (fig. 3). The inner shell is fabricated with aluminum honeycomb-core sandwich shell supported at discrete locations. The Apollo capsule was protected by the ablative Avcoat-5026-39H/CG TPS material (epoxy resin reinforced with quartz fibers and lightened with phenolic microballoons) that has an ablation temperature of about 1,200ºF (ref. 4). The ablation properties of the Avcoat-5026-39H/CG material are listed in table A1 (ref. 4).

Table A2 shows that the Apollo virgin TPS is 3.67 times heavier than the Space Shuttle tiles. In addition, it can be seen that the conductivity of the Apollo virgin TPS is 1.86 times the conductivity of the Shuttle tiles, and the heat capacity, ρc_p , is 8.18 times the Shuttle tile heat capacity. Also shown in this table is the thermal diffusivity, $\frac{k}{\left(\rho c_p\right)}$. It may be noted that thermal diffusivity is the ability of a material to absorb and prevent heat from penetrating to the substructures, and that the lower the numerical value the better its capability to perform this function. As shown, the thermal diffusivity of the Apollo virgin TPS is less than the diffusivity of the Shuttle tile by a factor of about 4.42. Therefore, for a given thickness and temperatures of 1,200ºF or less, the Apollo virgin TPS is capable of absorbing more heat than the Shuttle tile.

Table A1. Ablative properties of Avcoat 5026-39H/CG (the Apollo TPS material, ref. 4).

Combustion enthalpy	11,850 Btu/lb
Heat of vaporization	11,400 Btu/lb
Heat of decomposition	500 Btu/lb
Virgin density	1.9097×10^{-2} lb/in^3
Char density*	0.9549×10^{-2} lb/in^3

* The char density is approximately one-half of the virgin density.

Table A2. Comparison of thermal properties of Apollo TPS and Space Shuttle TPS tile at 1,200ºF (approximate ablation temperature).

	ρ, lb/in^3	c_p, Btu/lb-ºF	k, Btu/ in-sec-ºF	ρc_p, Btu/in^3-ºF	$k/(\rho c_p)$, in^2/sec
Apollo TPS	1.9097-2	0.655	0.3241-5	12.51-3	0.2591-3
Space Shuttle TPS	0.5208-2	0.294	0.1754-5	1.53-3	1.1455-3

Space Shuttle Orbiter Cargo Bay Doors

Composite materials (e.g., graphite/epoxy composite material) have matured greatly in the past 40 years since the Apollo capsule was designed, and have been widely applied to aerospace structures including the Space Shuttle Orbiter. As shown in figure 6, the Space Shuttle Orbiter cargo bay doors are fabricated with lightweight and high strength composite sandwich panels. The curved composite panels are fabricated with NOMEX honeycomb core (an excellent insulator) and graphite/epoxy face sheets (low heat conduction). The weight density of the graphite epoxy composite and aluminum are compared in table A3.

Table A3. Comparison of weight density of the graphite epoxy composite and aluminum.

Material	ρ, lb/in$_3$	ρ/ρ (aluminum)	weight saving, %
Aluminum	0.10130	1.00	0
Composite	0.05684	0.56	44

Note that the weight savings is nearly 44 percent when the composite sandwich panels are used instead of aluminum. This is a great weight savings for the Space Shuttle Orbiter.

Keep in mind also that the orbiter cargo bay doors are in the shadow zone (wake) of reentry heating, and covered with the high performance flexible NOMEX FRSI (Felt Reusable Surface Insulation). The FRSI performed very well in protecting the composite bay doors from overheating during the past STS flights (ref. 7). Since the conical afterbody of the CEV capsule is in the leeward zone, similar to the orbiter bay doors, NOMEX FRSI could also be a good candidate for the heat shield for the CEV capsule conical region.

In the past, the Space Shuttle Orbiter composite cargo bay doors exhibited excellent thermostructural performance and, therefore, this type of graphite/epoxy composite sandwich construction could be an excellent candidate structural concept for the CEV capsule wall structures.

APPENDIX B
INPUT THERMAL PROPERTIES

Radiation Properties

Radiation properties used for the space element (heat sink) are listed in table B1.

Table B1. Radiation properties of space element.

T, °R	ε	a	r
460	1	1	0

The 460° R is an averaged temperature of atmosphere during the high heating portion of the reentry flight (260,000 ft–150,000 ft altitude).

For internal radiation exchanges, the following radiation properties were used.

Thermal Properties

Materials thermal properties are presented in tables B2–B4. Shown are the thermal properties of 2219-T8XX aluminum, aluminum sandwich core, graphite/epoxy composite face sheets, NOMEX sandwich core, and Avcoat 5026-39/HC-G.

Table B2. Radiation properties for internal radiation exchanges.

T, °R	ε	a	r
530	0.667	0.667	0.333

Table B3. Thermal properties of 2219-T8XX aluminum (used in Space Shuttle Orbiter structure).

T, °R	ρ lb/in^3	c_p Btu/lb-°F	k_1 Btu/in-sec-°F	k_2 Btu/in-sec-°F	k_3 Btu/in-sec-°F
360	0.1013	0.183	1.4800-3	1.4800-3	1.4800-3
460	0.1013	0.195	1.5972-3	1.5972-3	1.5972-3
560	0.1013	0.206	1.7130-3	1.7130-3	1.7130-3
660	0.1013	0.215	1.8056-3	1.8056-3	1.8056-3
760	0.1013	0.222	1.8981-3	1.8981-3	1.8981-3
860	0.1013	0.228	1.9606-3	1.9606-3	1.9606-3
960	0.1013	0.234	2.0139-3	2.0139-3	2.0139-3
1060	0.1013	0.250	2.0694-3	2.0694-3	2.0694-3

Table B4. Thermal properties of aluminum sandwich core.

T, °R	ρ lb/in^3	c_p Btu/lb-°F	k_1 Btu/in-sec-°F	k_2 Btu/in-sec-°F	k_3 Btu/in-sec-°F
360	1.664-3	0.183	1.4800-3	1.4800-3	1.4800-3
460	1.664-3	0.195	1.5972-3	1.5972-3	1.5972-3
560	1.664-3	0.206	1.7130-3	1.7130-3	1.7130-3
660	1.664-3	0.215	1.8056-3	1.8056-3	1.8056-3
760	1.664-3	0.222	1.8981-3	1.8981-3	1.8981-3
860	1.664-3	0.228	1.9606-3	1.9606-3	1.9606-3
960	1.664-3	0.234	2.0139-3	2.0139-3	2.0139-3
1060	1.664-3	0.250	2.0694-3	2.0694-3	2.0694-3

REFERENCES

1. Ko, William L., *Heat Shielding Characteristics and Thermostructural Performance of Superalloy Honeycomb Sandwich Thermal Protection System (TPS)*, NASA/TP-2004-212024, 2004.

2. Ko, William, Leslie Gong, and Robert D. Quinn, *Reentry Thermal Analysis of a Generic Crew Exploration Vehicle Structure*, NASA/TM-2007-214607, 2007.

3. Lee, Dorothy B. John J. Bertin, and Winston D. Goodrich, *Heat-Transfer Rate and Pressure Measurements Obtained During Apollo Orbital Entries*, NASA TN D-6028, 1970.

4. Williams, S. D., and Donald M. Curry, *Thermal Protection Materials; Thermophysical Property Data*, NASA Reference Publication 1289, 1992.

5. Laub, B. and E. Venkatapathy, "Thermal Protection System Technology and Facility Needs for Demanding Future Planetary Missions," presented at the International Workshop on Planetary Probe Atmospheric Entry and Descent Trajectory Analysis and Science, Lisbon, Portugal, October 6–9, 2003.

6. Williams, S. D., Donald M. Curry, Stanley A. Bouslog, and William C. Rochelle, "Thermal Protection System Design Studies for Lunar Crew Module," AIAA-93-2843, July 1993.

7. Ko, William L., Robert D. Quinn, and Leslie Gong, *Finite-Element Reentry Heat-Transfer Analysis of Space Shuttle Orbiter*, NASA TP-2657, 1986.

8. Kinney, David J., "Aero-Thermodynamics for Conceptual Design," AIAA 2004-31, January 2004.

9. Kinney, David J., Joseph A. Garcia, and Loc C. Huynh, "Predicted Convective and Radiative Aerothermodynamic Environments for various Reentry Vehicles Using CBAERO," AIAA-2006-659, January 2006.

10. Tauber, Michael E., *A Review of High-Speed Convective Heat-Transfer Computational Methods*, NASA TP-2914, 1989.

11. Tauber, Michael E., and K. Sutton, "Stagnation-Point Radiative Heating Relations for Earth and Mars Entries," *Journal of Spacecraft and Rockets*, Vol. 28, No. 1, January–February 1991, pp 40–42.

12. Wright, Michael J., Graham Candler, and Deepak Bose, "Data-Parallel Line Relaxation Method for the Navier-Stokes Equations," *AIAA Journal*, Vol. 36, No. 9, 1998, pp 1603–1609.

13. Whetstone, W. D., *SPAR Structural Analysis System Reference Manual, System Level 13A, Vol. 1*, Program Execution, NASA CR-158970-1, 1978.

REPORT DOCUMENTATION PAGE

Form Approved
OMB No. 0704-0188

1. REPORT DATE *(DD-MM-YYYY)*	2. REPORT TYPE	3. DATES COVERED *(From - To)*
01-10-2007	Technical Memorandum	

4. TITLE AND SUBTITLE
Lunar Return Reentry Thermal Analysis of a Generic Crew Exploration Vehicle Wall Structures

5a. CONTRACT NUMBER

5b. GRANT NUMBER

5c. PROGRAM ELEMENT NUMBER

6. AUTHOR(S)
Ko, William L.; Tran, Van T.; and Bowles, Jeff

5d. PROJECT NUMBER

5e. TASK NUMBER

5f. WORK UNIT NUMBER

7. PERFORMING ORGANIZATION NAME(S) AND ADDRESS(ES)
NASA Dryden Flight Research Center
P.O. Box 273
Edwards, California 93523-0273

8. PERFORMING ORGANIZATION REPORT NUMBER
H-2768

9. SPONSORING/MONITORING AGENCY NAME(S) AND ADDRESS(ES)
National Aeronautics and Space Administration
Washington, DC 20546-0001

10. SPONSORING/MONITOR'S ACRONYM(S)
NASA

11. SPONSORING/MONITORING REPORT NUMBER
NASA/TM-2007-214627

12. DISTRIBUTION/AVAILABILITY STATEMENT
Unclassified -- Unlimited
Subject Category 34 Availability: NASA CASI (301) 621-0390 Distribution: Standard

13. SUPPLEMENTARY NOTES
Ko and Tran, NASA Dryden Flight Research Center; Bowles, NASA Ames Research Center

14. ABSTRACT

Thermostructural analysis was performed on generic crew exploration vehicle (GCEV) heat shielded wall structures subjected to reentry heating rates based on five potential lunar return reentry trajectories. The GCEV windward outer wall is fabricated with a graphite/epoxy composite honeycomb sandwich panel and the inner wall with an aluminum honeycomb sandwich panel. The outer wall is protected with an ablative Avcoat-5026-39H/CG thermal protection system (TPS). A "virtual ablation" method (a graphical approximation) developed earlier was further extended, and was used to estimate the ablation periods, ablation heat loads, and the TPS recession layer depths. It was found that up to 83–95 percent of the total reentry heat load was dissipated in the TPS ablation process, leaving a small amount (3–15 percent) of the remaining total reentry heat load to heat the virgin TPS and maintain the TPS surface at the ablation temperature, 1,200ºF. The GCEV stagnation point TPS recession layer depths were estimated to be in the range of 0.280–0.910 in, and the allowable minimum stagnation point TPS thicknesses that could maintain the substructural composite sandwich wall at the limit temperature of 300°F were found to be in the range of 0.767–1.538 in. Based on results from the present analyses, the lunar return abort ballistic reentry was found to be quite attractive because it required less TPS weight than the lunar return direct, the lunar return skipping, or the low Earth orbit guided reentry, and only 11.6 percent more TPS weight than the low Earth orbit ballistic reentry that will encounter a considerable weight penalty to obtain the Earth orbit. The analysis also showed that the TPS weight required for the lunar return skipping reentry was much more than the TPS weight necessary for any of the other reentry trajectories considered.

15. SUBJECT TERMS
Crew exploration vehicle, Heat transfer analysis, Lunar return reentry heating, Thermal protection system, Virtual ablation analysis

16. SECURITY CLASSIFICATION OF:			17. LIMITATION OF ABSTRACT	18. NUMBER OF PAGES	19b. NAME OF RESPONSIBLE PERSON
a. REPORT	b. ABSTRACT	c. THIS PAGE			STI Help Desk (email: help@sti.nasa.gov)
					19b. TELEPHONE NUMBER *(Include area code)*
U	U	U	UU	56	(301) 621-0390